UNIVERSITY OF OKLAHOMA

GRADUATE COLLEGE

# DESIGNING AND CHARACTERIZING NEGATIVE STIFFNESS DEVICES FOR APPARENT WEAKENING AND VERTICAL ISOLATION

A THESIS

SUBMITTED TO THE GRADUATE FACULTY

in partial fulfillment of the requirements for the

Degree of

MASTER OF SCIENCE

By

THOMAS M.N. CAIN
Norman, Oklahoma
2020

Downloaded from SHAREOK. Persistent Handle URL: https://hdl.handle.net/11244/324272

DESIGNING AND CHARACTERIZING NEGATIVE STIFFNESS DEVICES
FOR APPARENT WEAKENING AND VERTICAL ISOLATION

A THESIS APPROVED FOR THE
SCHOOL OF CIVIL ENGINEERING AND ENVIRONMENTAL SCIENCE

BY THE COMMITTEE CONSISTING OF

Dr. Philip Scott Harvey Jr., Chair

Dr. Royce W. Floyd

Dr. Jeffery S. Volz

© Copyright by THOMAS M.N. CAIN 2020
All Rights Reserved.

This thesis is dedicated first and foremost to the glory of God Almighty, who has blessed me with the intellect to explore His beautiful Mind by learning more about His Creation through this research.

It is also dedicated to my parents, Brendan and Teri, and my brothers Francis, Marcus, and Peter. I love you each, forever and always.

# Acknowledgements

I would like to thank numerous people for their support, guidance, and encouragement through my work on this thesis and in my time at OU.

This material is based upon work supported by the National Science Foundation under Grant No. NSF-CMMI-1663376. This support is greatly appreciated.

Dr. Royce Floyd and Dr. Jeffery Volz, for serving on my thesis committee, for being great professors for numerous courses, and for their contagious love of concrete.

Dr. Scott Harvey, of course, for his expertise and ideas that led to this work, for helping me slog through all of the math and coding, and for being such a tremendous professor that I was interested in beginning research with him.

My professors, teachers, and TAs in all of my courses at OU, especially in Civil Engineering.

My classmates who have helped me understand our course material and who I hope will continue to push me to be a better engineer, especially Patrick Lyhane who gave me an “in” with the Arch-E crowd and shared plenty of good laughs and good times throughout our time studying together.

My friends I made at random back in our freshman year at OU, who now have proven to be sure sources of joy and support, especially in these past few months.

My friends, mentors, ministers, missionaries, and parishioners I’ve known through St. Thomas More Catholic University Parish and in the OKC area at large, for a truly vibrant faith community that allowed me to thrive spiritually as I strove academically. A special thanks to Fr. Jim Goins, pastor, mentor, and friend, for your years of service

to STM and OU's Catholic students, and your support and friendship to me.

My aunts Mary Ann Nelles and Rosemarie Nelles whose generosity knows no equal and whose prayers are surely at least half the reason I am where I am today.

All of my aunts, uncles, and cousins on both the Cain and Nelles sides, for your love, friendship, and care for me; and my grandparents who I know have supported me with prayers from above.

My brothers, Peter, Marcus, and Francis, for your love and friendship that has only grown stronger as we've been further spread apart across the globe.

My parents, for their love and support, financially and spiritually. Words cannot express the gratitude I owe you, but I'd like to make a special acknowledgement of everything you gave up, handed on, pushed me to do, kept me from, and taught me.

And finally, *Deo gratias*!

# Table of Contents

**Acknowledgments** . . . . . **v**

**Table of Contents** . . . . . **vii**

**List of Figures** . . . . . **ix**

**List of Tables** . . . . . **xii**

**Abstract** . . . . . **xiii**

**1 Introduction** . . . . . **1**
1.1 Overview . . . . . 1
1.2 Previous Approaches to Seismic Mitigation . . . . . 1
1.2.1 Passive Approaches to Seismic Mitigation . . . . . 2
1.2.2 Alternative Approaches to Seismic Mitigation . . . . . 3
1.3 Negative Stiffness Devices . . . . . 4
1.3.1 Negative Stiffness for Apparent Weakening . . . . . 4
1.3.2 Negative Stiffness in Vertical Isolation . . . . . 10
1.4 Summary . . . . . 14

**2 Smooth Negative Stiffness Device** . . . . . **16**
2.1 Overview . . . . . 16
2.2 Load-Deflection Relation of Smooth Negative-Stiffness Device . . . . . 16
2.2.1 A Note on Scalability . . . . . 20
2.3 Experimental Prototype . . . . . 21
2.4 Experimental Results . . . . . 23
2.4.1 Characterization Tests . . . . . 23
2.4.2 Harmonic Excitation . . . . . 25
2.4.3 White Noise Excitation . . . . . 28
2.5 Simulated Earthquake Response . . . . . 29
2.5.1 Simulated Structure and Device Parameters . . . . . 29
2.5.2 Ground Motions used in Numerical Simulations . . . . . 31
2.5.3 Simulation Results . . . . . 32
2.6 Summary . . . . . 38

**3 Buckled-Strut Vertical Isolation System** . . . . . **40**

3.1 Overview . . . 40
3.2 Lateral Load-Deflection Relation of a Buckled Strut . . . 40
3.2.1 Negative Stiffness Approximation with Two Terms . . . 45
3.2.2 Load-Deflection Relation with Three Terms . . . 49
3.3 Buckled-Strut Vertical Isolation System . . . 55
3.3.1 BSVIS Benefits . . . 57
3.4 BSVIS Prototype . . . 59
3.5 Experimental Results . . . 60
3.5.1 Static Testing . . . 60
3.6 Design Recommendations . . . 63
3.7 Summary . . . 64

**4 Summary, Conclusions, and Future Work . . . 66**
4.1 Summary and Conclusions . . . 66
4.2 Future Work . . . 67

**Bibliography . . . 68**

**A Buckling under Imperfections . . . 73**
A.1 Background . . . 73
A.2 Initially Bent, Eccentrically Loaded Column . . . 74
A.2.1 Effect of Imperfections on Midspan Deflection . . . 75
A.3 Experiments . . . 77
A.3.1 Experimental Setup . . . 77
A.3.2 Experimental Results . . . 79
A.3.3 A Note on Repeatability . . . 81
A.3.4 Circular Arc Initial Imperfection . . . 82
A.4 Concluding Remarks . . . 83

# List of Figures


1.1 Drawing of the friction-based negative stiffness damper . . . . . 4
1.2 Idealized force-displacement curves of NSD behavior . . . . . 6
1.3 Adaptive negative stiffness system . . . . . 7
1.4 Force-displacement curves of components of the ANSS . . . . . 7
1.5 Experimental force-deformation loops of the ANSS, experimental structure, and the structure-ANSS assembly subjected to Kobe earthquake ground motions . . . . . 8
1.6 Small-scale prototype of RBMAP device . . . . . 8
1.7 Simulated force-displacement profiles of an isolated bridge (IB), the bridge equipped with the RBMAP, and the bridge equipped with the modified RBMAP . . . . . 9
1.8 Variable negative stiffness device prototype in test assembly . . . . . 9
1.9 (a) Experimental and theoretical results of the VNSD; (b) Analytical force-displacement profiles for the structure, the VNSD (ZNZ1), and the structure-device system . . . . . 10
1.10 Spring-damper vertical isolator and dimensions (left) and view of experimental set up on shake table of triple FPs on the spring-damper (right); Source: Lee and Constantinou (2018) . . . . . 12
1.11 (a) Schematic of piecewise-constant restoring force vertical isolator and (b) force-deflection profile of the isolator with u=¬0 at the static equilibrium position . . . . . 12
1.12 Views of the VIS of the 3D isolation device of Cimellaro et al. (2018): (a) A 3D view of the vertical isolator; (b) A radial section through the device showing the spring and lever assembly . . . . . 13
1.13 (a) Schematic of the quasi-zero stiffness system and (b) force-displacement profile of the components of the QZS vertical isolator . . . 14

2.1 Geometry and configuration of (a) PNP and (b) NP devices. . . . . 17
2.2 (a) Theoretical normalized load-deflection relation of an SNSD in parallel with a linear-elastic structure having stiffness $K_e$. (b) The associated rotations in the PNP and NP devices based on Eq. (2.8), with the nonlinear relationships (—) given by Eq. (2.6) for comparison . . . . . 19
2.3 Experimental prototype of an SNSD: Left, the NP device in the foreground; Right, the PNP device in the foreground. . . . . 21

2.4 Dimensioned drawings of experimental prototype (with only one device shown). . . . . 23
2.5 (a) Experimental and (b) theoretical load-deflection relations of the elastic structure, SNSD component devices, and combined structure-SNSD system. . . . . 24
2.6 Experimental system installed on shake table with connected accelerometers. . . . . 26
2.7 Transmissibility under harmonic excitation of varying peak ground acceleration, $a_{go}$: (a–c) experiments for $a_{go}$ = (a) 5, (b) 10, and (c) 15%$g$ and (d) theory. . . . . 26
2.8 (a) Time history of the white noise excitation to which the experimental structure-SNSD system was subjected, and (b) response of the system. . 29
2.9 Peak structure acceleration under white noise excitation of varying intensity. . . . . 29
2.10 Comparison of ideal, target, and fitted load-deflection relations used in the SNSD simulations: (a) ZNP and (b) ZNZ configurations . . . . . 32
2.11 Historic ground motion time histories (unscaled). . . . . 33
2.12 Linear elastic response spectra (5% damped) for (a) historic and (b–f) synthetic ground motions (GMs) . . . . . 34
2.13 Normalized load-deflection responses for (a) Lucerne, (b) Erzincan, and (c) Rinaldi . . . . . 37
2.14 Average change in performance index $J_i$ (Table 2.4) due to the addition of an SNSD, using the performance of a system without an SNSD (BS+VD) to benchmark those with SNSDs (BS+VD+ZNP and BS+VD+ZNZ). . . . . 38

3.1 A schematic of an assembled BSVIS consisting of a buckled strut and a linear spring of stiffness $k$ supporting a payload of mass $m$ . . . . . 41
3.2 Geometry and description of a buckled strut: (a) an initially undeformed strut of length $L$; (b) the strut after an end shortening of $\varepsilon = \varepsilon_0$ resulting in the initial deflected shape $v_0(x)$ with lateral rise $H$; (c) the strut when a lateral constraint is enforced such that $v(\bar{x}) = A$. . . . . 41
3.3 Boundary conditions and lateral constraints considered . . . . . 48
3.4 Shape functions $\psi_1(x)$ and $\psi_2(x)$ assumed in two-term expansion . . . . 48
3.5 (left) Solutions for $Q_1$ and $Q_2$ normalized by rise $H$, and (right) the resulting load-deflection relations for Cases a–d (a–d). For Case d, both the symmetric (—) and rotationally symmetric (-··-·) solutions are shown, corresponding to Cases d(i) and d(ii), respectively, in Fig. 3.4(d). 50
3.6 Load-deflection relations for Case c. . . . . 51
3.7 Detached load-deflection relations for Case d(i). . . . . 51

3.8 Normalized lateral load-deflection relation of a buckled strut for $\bar{x}$ = (a) $0.499L$, (b) $0.49L$, and (c) $0.45L$ using a three-term approximation of $v(x)$, as well as the two-term approximation for $\bar{x} = 0.499L$ (d). The black and gray lines are detached equilibria, each with stable (—) and unstable (– – –) branches. . . . . 55
3.9 Normalized load-deflection relations of BSVISs composed of a pin-ended buckled strut (Case c with $\bar{x} \approx 0.5L$) in parallel with linear springs having different relative stiffnesses, $\kappa = k/\tilde{k}_{\text{neg}}$. Unstable solutions are not shown. . . . . 56
3.10 BSVIS load-deflection relationship. . . . . 58
3.11 Photograph of the prototype of a BSVIS (a) various components labeled and (b) close-up of the pinned connection and the spring-to-platform connection . . . . . 60
3.12 Photograph of the BSVIS prototype shown connected to the universal testing machine . . . . . 61
3.13 Experimental load deflection data for tests (a) without and (b) with springs connected. Slopes for different portions of the relations are denoted on each plot . . . . . 61

A.1 Initially bent column under eccentric load. . . . . 74
A.2 Load-deflection curves of eccentrically loaded, pre-cambered columns. . 76
A.3 (a) Test specimen nominal dimensions and (b) 3D-printed specimens. . 78
A.4 Images of the experimental setup (a) and pin fixture (b). . . . . 79
A.5 Compressive load versus end shortening for imperfection amplitude $a$ = (a) 3.175, (b) 6.350, and (c) 9.525 mm with varying load eccentricity to imperfection amplitude ratio $e/a$. Sign of midspan deflection is distinguished by line style: $\delta < 0$ (dashed) and $\delta > 0$ (solid). . . . . 80
A.6 Regions of positive and negative midspan deflection $\delta$ in the parametric space (load eccentricity $e$ versus imperfection amplitude $a$) based on Eq. (A.7), with comparison to experimental results ($\delta < 0$: ∘; $\delta > 0$: +). . . . 81

# List of Tables


2.1 Experimental SNSD dimensions and parameters. . . . . 23
2.2 Dimensions and parameters of the fitted SNSDs. . . . . 31
2.3 Summary of historic earthquake motions (unscaled). . . . . 33
2.4 Definitions of the performance indices. . . . . 34
2.5 Performance indices from the historic GM simulations . . . . . 35
2.6 Performance indices from the synthetic GM simulations . . . . . 36

3.1 Lateral negative stiffness values $k_{\text{neg}}$ for different boundary conditions and lateral constraints. . . . . 47

A.1 Fourier coefficients $a_n$ ($n = 1, 3, 5, 7$) for a circular arc with span $L =$ 190.5 mm and varying amplitude $a$. . . . . 83

# Abstract

Nonlinear systems leveraging the effects of negative stiffness can exhibit beneficial qualities for passive seismic mitigation in structures. Such systems can be achieved by placing nonlinear devices displaying negative stiffness in parallel with linear positive stiffness systems such as a structure or spring. This thesis presents research into two such systems: (i) a device which causes apparent weakening in a structure subjected to horizontal ground motions and (ii) an isolation system to protect building contents from vertical seismic effects.

Apparent weakening is the softening of a structure's apparent stiffness by adding negative stiffness to the overall system via negative stiffness devices. Apparent weakening is an elastic effect that has the benefit of reducing the peak accelerations and base shears induced in a structure due to a seismic event without reducing the main structural strength. The smooth negative stiffness device (SNSD) presented in this thesis consists of cables, pulleys, and extension springs. A nonlinear mathematical model of the load-deflection behavior of the SNSD was developed and used to determine the optimal geometry for such a device. A prototype device was designed and fabricated for installation in a bench-scale experimental structure, which was characterized through static and dynamic tests. A numerical study was also conducted on two other SNSD configurations designed to achieve different load-deflection relations for use in an inelastic model building subject to a suite of historic and synthetic ground motions. In both the experimental prototype and the numerical study, the SNSDs successfully produced apparent weakening, effectively reducing accelerations and base shears of the

structures.

The buckled-strut vertical isolation system (BSVIS) presented in this thesis combines the non-linear behavior of a laterally-loaded buckled strut with a linear spring. The lateral load-deflection relation for a buckled strut, which is nonlinear and displays negative stiffness, was investigated for various conditions to two- and three-term approximations of the deflected shape of a strut. This relation and the linear positive effect of a spring were superimposed to give the load-deflection relation of a BSVIS. An experimental prototype was fabricated and subjected to static tests. These tests confirmed the validity of the model and the effectiveness of adding a spring in parallel with a buckled strut to achieve isolation-level stiffness. Based on the theoretical and experimental findings, a design guide is proposed for the engineering of a BSVIS to protect a payload from vertical seismic content.

# Chapter 1
# Introduction

## 1.1 Overview

Seismic activity has historically resulted in large amounts of damage to structures lacking proper seismic detailing or seismic mitigation systems (Moroni et al., 2012), and the threat of large earthquakes always looms, even in states such as Oklahoma which, until recently, have not been considered areas of high seismic activity (Harvey et al., 2018). Whether a structure is a bridge, a building, or a transmission line tower, protecting the structure and the people who use it is of utmost concern to engineers involved in seismic design. Also important is protecting sensitive equipment and components such as server towers or microscopes from vibrations induced by earthquakes. The use of negative stiffness to cause nonlinear-elastic behavior for seismic mitigation is attested to in the literature, and is reviewed in the remainder of this chapter.

## 1.2 Previous Approaches to Seismic Mitigation

Many advanced techniques to mitigate a structure's response to seismic loading take one of two approaches: supplemental damping or base isolation; and these can be active, passive, or systems somewhere in between. Other approaches have gained popularity recently, among them the use of negative stiffness in seismic applications. The need for effective vertical isolation has also become of greater interest. Traditional methods of seismic mitigation, alternative methods, and the recent development of negative stiffness

devices (NSDs) and vertical isolation systems (VISs) as an answer to these methods' shortcomings are reviewed in the following sections.

### 1.2.1 Passive Approaches to Seismic Mitigation

Typical approaches to mitigating the seismic response of a structure are passive seismic dampers and base isolation. Seismic mitigation techniques are part of the subject of structural control, which is the design of building systems to dissipate or redirect energy in a way in which the structure is not damaged (Saaed et al., 2015). Structural control can be broken into four broad categories: passive, semi-active, active, and hybrid systems. This research will focus on passive systems, which can be further divided into the subgroups of seismic isolation and energy dissipation devices (Saaed et al., 2015). While some dampers and isolation techniques bleed over into the semi-active or active categories, damping and isolation are largely encompassed within the two subgroups of passive systems.

Many seismic dampers have been developed, characterized, and implemented in practice since the 1970s (Kelly et al., 1972; Robinson and Tucker, 1976). Passive damping devices come in many forms including, but not limited to, viscous fluid dampers, viscoelastic solid dampers, metallic dampers, and friction dampers (Symans et al., 2008). Adding supplemental damping is a popular and efficient means of dissipating energy from seismic loading that may otherwise lead to damage in the structure (Symans et al., 2008).

Base isolation for the seismic protection of structures consists of placing flexible devices at the base of a structure to decouple its motion from the ground's motion (Warn and Ryan, 2012). This decoupling shifts the structure's natural period to a longer period, which reduces floor accelerations and inter-story drifts caused by an earthquake. Common types of isolation systems can be divided into elastomeric and sliding devices (Warn and Ryan, 2012). Rolling-type isolation systems are also common base isolation

solutions, but are typically limited in application to equipment isolation, rather than used in structures (Harvey and Kelly, 2016).

These traditional techniques have their disadvantages. As effective as damping may be in seismic mitigation, large damping ratios can increase base shears within structures (Pasala et al., 2013). While shifting the period of a structure through base isolation can protect it from high frequency seismic content, this can lead to increased displacements at the isolation interface (Warn and Ryan, 2012). This is often remedied by the application of a damper, but large damping ratios have the adverse effect of increasing absolute acceleration in such systems (Iemura and Pradono, 2009).

### 1.2.2 Alternative Approaches to Seismic Mitigation

Other approaches to mitigate seismic effects include active, semi-active, and hybrid control systems. Active control techniques are those "in which the motion of a structure is controlled or modified by means of the action of a control system through some external energy supply" (Soong, 1988). High costs and high power demands are obstacles to the viability of active control (Spencer and Sain, 1997). Semi-active control uses an actuator to modify the behavior of a passive device (Saaed et al., 2015). Semi-active systems still need a power supply for sensors and actuators, but the demand is much less than that in active systems, because the actuators of semi-active devices do not apply forces directly to the structure. Hybrid control systems implement combinations of passive, semi-active, and active devices in series or in parallel to leverage the benefits of each group (Saaed et al., 2015). Each of these schemes of alternative structural control has its own shortcomings for seismic mitigation.

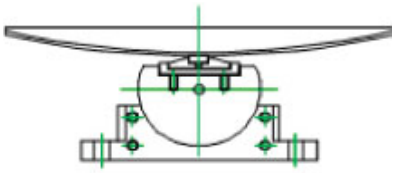


**Figure 1.1:** Drawing of the friction-based negative stiffness damper; Source: Iemura and Pradono (2009)

## 1.3 Negative Stiffness Devices

### 1.3.1 Negative Stiffness for Apparent Weakening

New approaches, including using negative stiffness to achieve apparent weakening, have been investigated to avoid the adverse effects and insufficiencies of active, semi-active, and passive devices (Pasala et al., 2013). Negative stiffness assists rather than resists deflection of the structure. Negative stiffness devices (NSDs) are devices with geometric configurations such that negative stiffness is added to the structure when it displaces.

An early attempt to make an NSD was the proposal of pseudo-negative stiffness dampers (PNSDs) which produce negative stiffness hysteretic loops (Iemura and Pradono, 2009). The PNSDs are not true NSDs because a damper is unable to assist the motion of the structure, but rather they produce behavior similar to the addition of negative stiffness. An example of such a PNSD is a friction-based passive negative stiffness damper (Iemura and Pradono, 2009). This device, pictured in Fig. 1.1, was able to produce negative stiffness hysteretic loops without active or semi-active control (i.e., a passive system) due to the convex shape of the friction plate.

Linear passive NSDs have been developed for varying applications. When combined with passive supplemental damping, the NSD of Chen et al. (2015) was proven to increase the amount of damping in a vibrating cable. This NSD consisted of a pre-compressed spring which had approximately linear negative stiffness. Such an NSD can be thought of as a weakening device, since its purpose is to increase displacement, in

this case across the damper to allow an increase in damping.

PNSDs and linear NSDs have beneficial results, but NSDs with variable stiffness can provide greater passive control of the structure's behavior while avoiding weakening the system under small displacements. Variable stiffness devices also allow for the development of apparent weakening. The current practice of designing buildings for seismic events, even with supplemental damping or other mitigation approaches, allows for inelastic (post-yield) action to reduce structural accelerations and interstory drifts. Apparent weakening is defined as "the softening of the structure's apparent stiffness through the addition of negative stiffness at a displacement that is smaller than the structure yield displacement" (Walsh et al., 2018). Apparent weakening achieves the benefits of a yielding structure (reduced structural accelerations and interstory drifts) without requiring the main structure to undergo yielding, altering the original structural system, or permanently damaging the structure (Pasala et al., 2013). Idealized force-displacement curves of a structure equipped with a variable (nonlinear) NSD are shown in Fig. 1.2. The light gray curve describes the behavior of a typical structure, without modification from an NSD, that weakens at its yield displacement, $u_y$. The dark gray curves describe the behavior of the NSD, which—under small deflections—adds neither negative nor positive stiffness. As the structure begins to deflect further, the NSD has a negative stiffness past $u'_y$, the prescribed apparent yield displacement. The black curves illustrate the behavior of the structure-device (SD) system. The apparent weakening behavior is clearly shown by the change in total stiffness at $u'_y$. The two profiles show different design possibilities of NSDs: (a) shows an NSD that adds positive stiffness to, or strengthens, the structure after a certain deflection has been reached (here, at the structure's yield point $u_y$), while (b) shows an NSD that adds no negative or positive stiffness after $u_y$. Various NSDs have been designed to try to attain these idealized curves, and some examples are reviewed below.

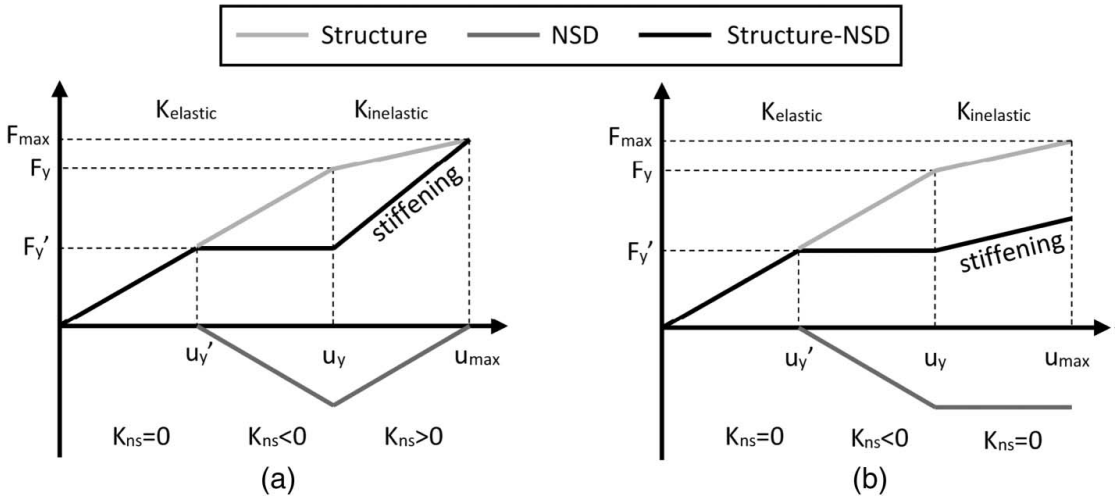



**Figure 1.2:** Idealized force-displacement curves of NSD behavior; Source: Walsh et al. (2018)

A variable passive NSD was developed and dubbed the adaptive negative stiffness system (ANSS) (Pasala et al., 2013, 2014; Sarlis et al., 2013). The ANSS, pictured in Fig. 1.3, consists of a pre-compressed spring, a toggle arm, and two other compression springs, all fit within a double-chevron brace configuration. When the structure undergoes deflection, the toggle arm rotates, causing the pre-compressed spring to produce a moment. This is the negative stiffness action of the device. The two compression springs at the bottom of the device, termed the gap-spring assembly (GSA), serve to cancel the negative stiffness contribution at small deflections. The force-displacement profiles of the pre-compressed spring, the GSAs, and the complete ANSS are shown in Fig. 1.4. The structure-ANSS assembly was subjected to Kobe earthquake ground motions and produced the experimental force-displacement curves shown in Fig. 1.5. The structure-ANSS assembly achieves apparent weakening before the structure's true yield point, which is shown by the dotted black line in Fig. 1.5 as it follows a relatively flat path beyond 0.5 in. of deflection (Pasala et al., 2014).

Another approach to achieving negative stiffness in structures is found in the rotation-based mechanical adaptive passive (RBMAP) device (Attary et al., 2017). The device, pictured in Fig. 1.6, consists of three geared wheels with internal pre-torqued

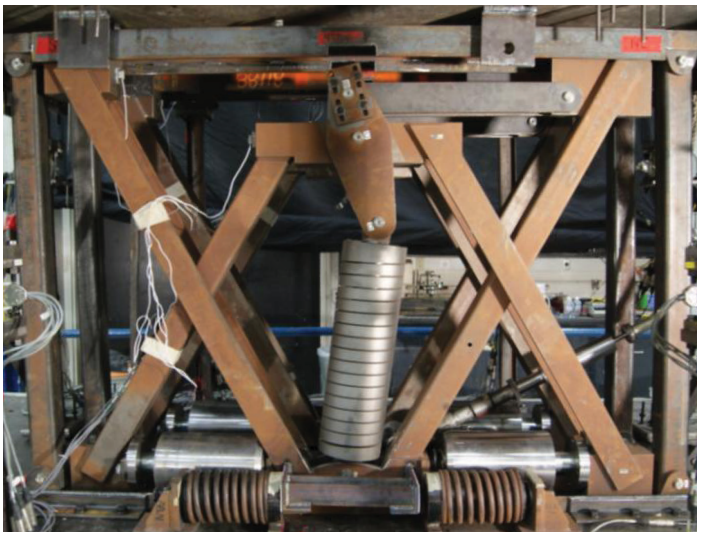


**Figure 1.3:** Adaptive negative stiffness system; Source: Pasala et al. (2014)

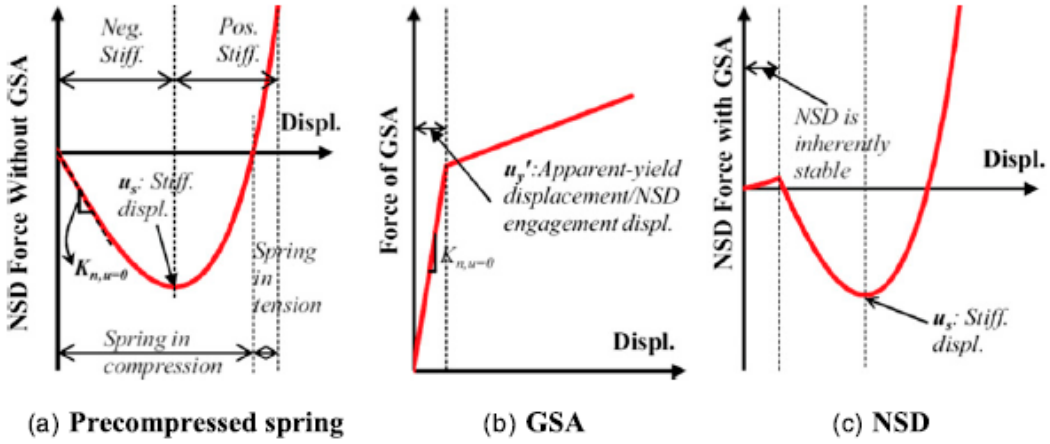



**Figure 1.4:** Force-displacement curves of components of the ANSS; Source: Sarlis et al. (2013)

torsional springs. The middle wheel is connected to one floor of the structure through a pinned connecting arm, and the outer wheels are fixed to another floor. Under small deflections, the wheels are not engaged, allowing the structure to respond naturally. When the structure experiences larger inter-story drift, the middle wheel moves over and engages one of the two outer gears, which then assists the deflection of the structure and adds negative stiffness. An analytical model of the RBMAP was used in simulations, and initially undesirable results were obtained. The engagement of the negative stiffness was too abrupt, and excessively large negative stiffness occurred at

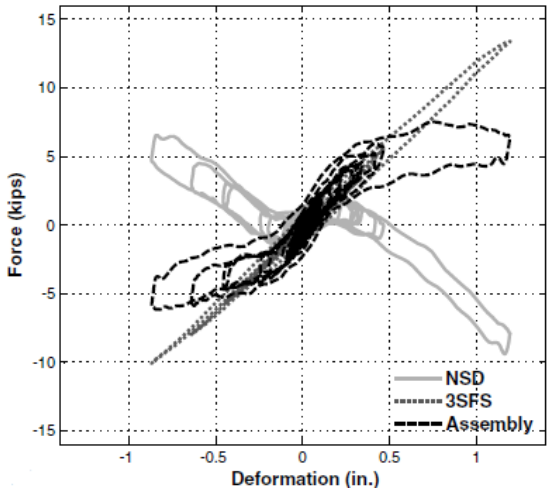



**Figure 1.5:** Experimental force-deformation loops of the ANSS, experimental structure, and the structure-ANSS assembly subjected to Kobe earthquake ground motions; Source: Pasala et al. (2014)

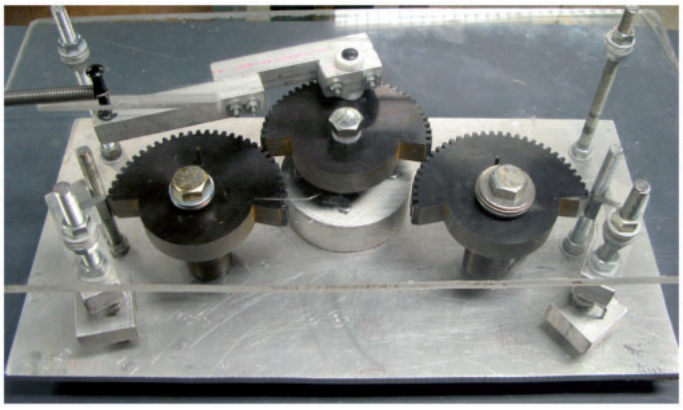


**Figure 1.6:** Small-scale prototype of RBMAP device; Source: Attary et al. (2017)

large deflections. The model was modified to include additional springs that would cancel out the unwanted behavior, and simulations were again performed. The resulting force-displacement profiles are shown in Fig. 1.7. The profile of the modified device resembles the behavior represented in Fig. 1.2(a).

A third NSD was designed with geared wheels and extension springs (Walsh et al., 2018). As shown in Fig. 1.8, this NSD uses two pre-tensioned springs on two pairs of geared wheels. The "N-N Gear Pair" provides negative stiffness, and the "N-P Gear Pair" negates the negative stiffness at small deflections, and then aids the N-N pair in

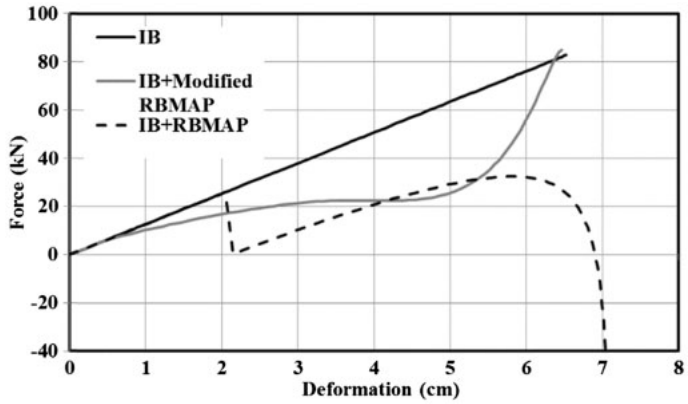



**Figure 1.7:** Simulated force-displacement profiles of an isolated bridge (IB), the bridge equipped with the RBMAP, and the bridge equipped with the modified RBMAP; Source: Attary et al. (2017)

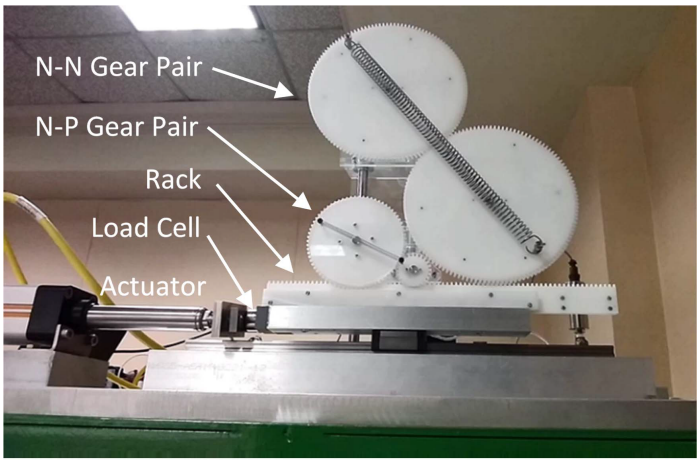



**Figure 1.8:** Variable negative stiffness device prototype in test assembly; Source: Walsh et al. (2018)

providing negative stiffness. The relative sizes of the gears and springs of this device were modified to produce both force-displacement curves shown in Fig. 1.2. This NSD was experimentally tested in the set-up shown in Fig. 1.8 and the experimental results, as well as theoretical curves, are shown in Fig. 1.9(a). It was also analytically modeled in a structure, and the resulting hysteretic curves are shown in Fig. 1.9(b).

All the presented NSDs share some important characteristics. First, under small deflections, the NSDs do not affect the response of the structure. This is important so that excessive deflections are not induced when relatively small lateral loads, such as small wind loads, act on the structure. Second, the NSDs achieve apparent weakening

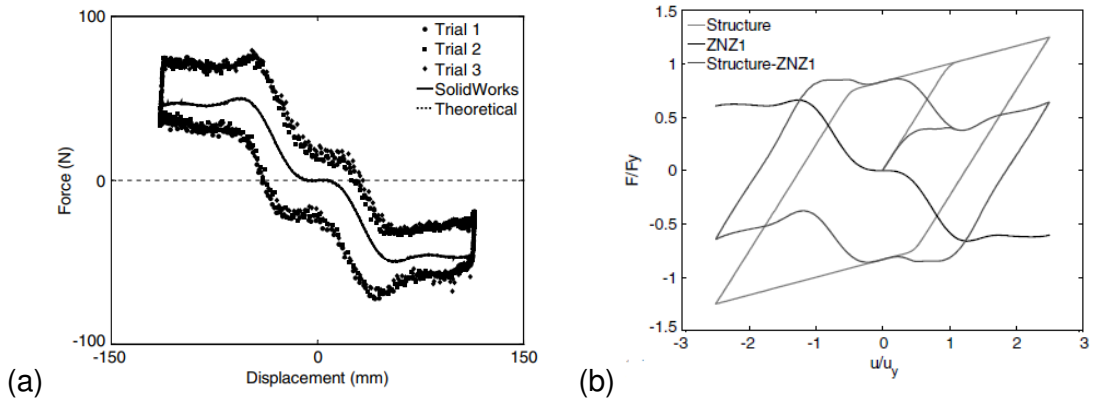



**Figure 1.9:** (a) Experimental and theoretical results of the VNSD; (b) Analytical force-displacement profiles for the structure, the VNSD (ZNZ1), and the structure-device system; Source: Walsh et al. (2018)

at a certain prescribed deflection. Third, this apparent weakening does not continue into very large deflections, and the structure-device systems eventually stiffen.

These NSDs show promise for implementing apparent weakening, but more progress can be made. Of the devices presented, only the ANSS has been characterized in a full-scale experimental test. Additionally, these devices each have geometry that rely on complicated spring configurations or geared parts, which may impede constructability, reliability, or serviceability of these designs. The ANSS and RBMAP also have components which physically engage and disengage, which raises a durability concern because of repeated impacts due to an excitation, and the VNSD uses a rack-and-pinion design to transfer the linear motion of the structure into the rotation of the device. Rack-and-pinion applications are not widespread in structural contexts.

### 1.3.2 Negative Stiffness in Vertical Isolation

Another potential application of negative stiffness for structural control is in the function of vertical isolation. Vertical isolation is a form of base isolation that, rather than decoupling a structure or piece of equipment from horizontal ground movement, seeks to decouple it from the vertical component of ground motion. Vertical ground motion has previously been relatively unconsidered in structural design, but it has been explicitly

incorporated into the load combinations in the latest version of ASCE *Minimum Design Loads and Associated Criteria for Buildings and Other Structures* (ASCE, 2017). Vertical accelerations can have significant impacts on buildings as well as equipment within buildings. Additional motivation for vertical isolation has arisen from some horizontal isolation techniques that have been shown to impart vertical accelerations that are not negligible (Harvey, 2015). Vertical accelerations have also been shown to be significantly amplified through horizontal isolation systems (Ryan et al., 2016). Negative stiffness has been used to achieve vertical isolation in commercial applications (Platus, 1992).

Linear vertical isolation systems (VISs) have been difficult to develop as an isolation-level (very low) stiffness at small deflections leads to undesirable settling due to the gravitational self-weight of the isolated body. An example of this is work done by Lee and Constantinou (2018), who tested triple friction pendulum (FP) horizontal isolators in combination with vertical isolators consisting of coil springs and linear viscous dampers, pictured in Fig. 1.10. The system, which had a vertical frequency of 2 Hz, had a static vertical displacement of 60 mm and a capacity for an additional 40 mm of dynamic displacement. Experimental testing found this 2 Hz frequency to be undesirable, but reducing the frequency of the VIS further would have increased the static displacement, thereby limiting the dynamic displacement capacity and rendering the device not as effective (Lee and Constantinou, 2018).

The inherent difficulties of linear vertical isolators necessitate the development of nonlinear VISs. A VIS having piecewise-constant restoring force was developed using two sets of constant-force springs supporting two different platforms (Fig. 1.11(a)), resulting in two different regions of very low stiffness (Fig. 1.11(b)) (Araki et al., 2009). The platforms are described as a bar and a table in Fig. 1.11(a). This system showed large reductions in peak responses without excessive static deflections and had a self-

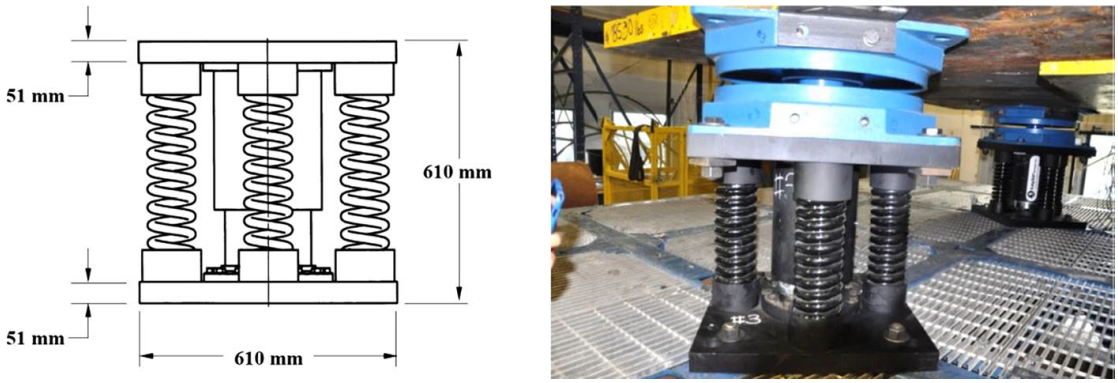



**Figure 1.10:** Spring-damper vertical isolator and dimensions (left) and view of experimental set up on shake table of triple FPs on the spring-damper (right); Source: Lee and Constantinou (2018)

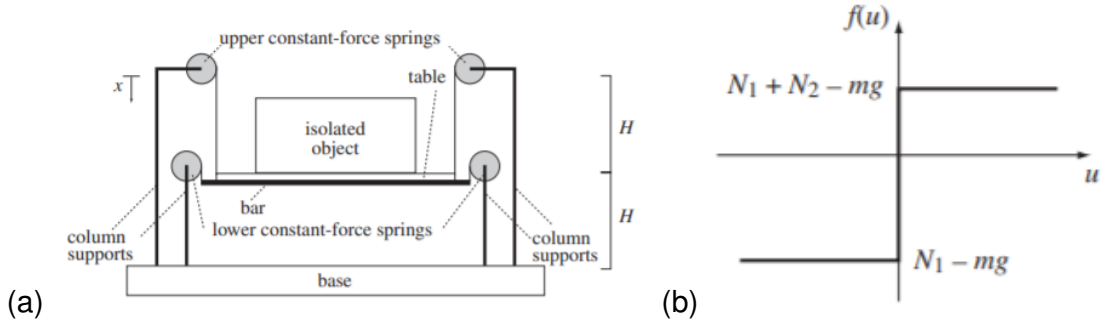



**Figure 1.11:** (a) Schematic of piecewise-constant restoring force vertical isolator and (b) force-deflection profile of the isolator about its static equilibrium position; Source: Araki et al. (2009)

centering capacity. A major drawback of this design is the impact between the bar and the table, which was the main source of measured peak response accelerations even when different mitigation strategies such as placing a flexible rubber layer between the platforms were tried (Araki et al., 2009). Additionally, while the constant-force springs that provide the vertical restoring force are compact, the need to hang the isolated object from column supports does not provide a low-profile system and could cause issues with horizontal motion responses.

Cimellaro et al. (2018) developed a three-dimensional isolation system that uses an NSD for the vertical isolation component. A schematic of the NSD, which highly resembles the ANSS, is presented in Fig. 1.12. The pre-compressed spring causes further deflection when vertical displacements occur across the device, and this effect is can-

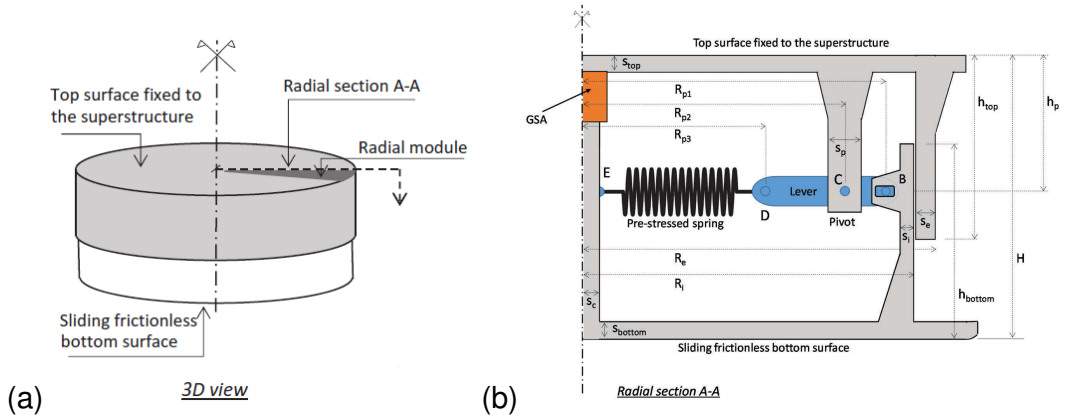



**Figure 1.12:** Views of the VIS of the 3D isolation device of Cimellaro et al. (2018): (a) A 3D view of the vertical isolator; (b) A radial section through the device showing the spring and lever assembly; Source: Cimellaro et al. (2018)

celed by a gap-spring assembly (GSA) at low deflections to prevent unwanted settling from gravity loads. The horizontal isolators for this 3D system were rubber bearings in parallel with the NSD. Numerical simulations of this device showed reduced vertical accelerations when this device was installed compared to when a structure was only horizontally isolated (Cimellaro et al., 2018). This device was effective in reducing vertical accelerations, but it does rely on a similar GSA configuration as did the ANSS. This means that the GSA must engage and disengage when the device is excited, and at the high frequencies under consideration for vertical isolation, this could cause greater concerns than in the horizontal motion of the ANSS.

Another recent nonlinear VIS is a quasi-zero stiffness (QZS) vertical isolator consisting of linear springs in parallel with disk springs which have nonlinear stiffness, proposed by Zhou et al. (2019). The disk springs have a region of negative stiffness, which is balanced by the linear spring to provide a sufficient static deflection at the static equilibrium point with a near-zero stiffness under a dynamic vertical excitation either side of equilibrium. The system stiffens at large deflections, and contact is never lost between the parts of the system (Zhou et al., 2019). The system and corresponding force-deflection profile is presented in Fig. 1.13. This system presents an effective and

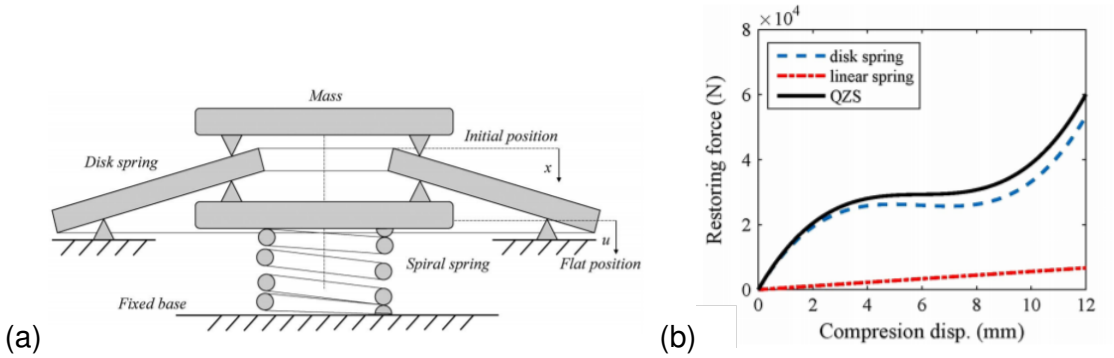



**Figure 1.13:** (a) Schematic of the quasi-zero stiffness system and (b) force-displacement profile of the components of the QZS vertical isolator; Source: Zhou et al. (2019)

low-profile solution for nonlinear vertical isolation.

## 1.4 Summary

Negative stiffness can be effectively used to produce nonlinear-elastic systems. Applications of nonlinear negative stiffness for seismic protection in apparent weakening and vertical isolation are attested to in the literature. Previously developed NSDs present effective solutions to limitations in other seismic mitigation strategies, yet many drawbacks are still present in these designs. This thesis presents research into the development of a novel smooth negative stiffness device (SNSD) intended to reduce damage to a structure from an earthquake (Chapter 2), as well as a buckled-strut vertical isolation system (BSVIS) intended to achieve effective vertical isolation of equipment within a building (Chapter 3). Both devices exploit elastic nonlinear behavior, induced by the integration of negative stiffness, to achieve beneficial responses to an earthquake ground motion. The SNSD developed in the present thesis attempts to overcome some of the drawbacks found in other NSDs for apparent weakening. The nonlinear BSVIS developed using a laterally-loaded, post-buckled strut—consistently shown to be a source of nonlinear negative stiffness (Thompson and Hunt, 1983; Lee et al., 2007; Kashdan et al., 2012; Harvey and Virgin, 2015)—in parallel with linear springs can achieve effective vertical isolation. This thesis is concluded by a summary of the work presented and

suggestions on future directions for research on these topics (Chapter 4).

# Chapter 2
# Smooth Negative Stiffness Device*

## 2.1 Overview

This chapter lays out the development of a novel smooth negative stiffness device (SNSD) as another alternative to effecting negative stiffness and apparent weakening within a structure. This device is so named because it smoothly transitions between the different stages of stiffness modification. It does so with a system of cables and pulleys to transfer translational motion from the structure to the device, rather than the rack-and-pinion design of Walsh et al. (2018). The load-deflection relationship of the SNSD is described first (Section 2.2), followed by a description of the design and fabrication of an experimental prototype of such an SNSD (Section 2.3). The prototype was subject to experimental testing and the results of static, harmonic, and white noise testing are presented (Section 2.4). Numerical simulations were conducted for an SNSD in an inelastic building subject to multiple ground motions, and these results are presented (Section 2.5) before this chapter is concluded (Section 2.6).

## 2.2 Load-Deflection Relation of Smooth Negative-Stiffness Device

The proposed SNSD, which would be in parallel with a structure of elastic stiffness $K_e$, is composed of a positive-negative-positive (PNP) stiffness device (Fig. 2.1(a)) and a

*This chapter is published as Cain et al. (2020).

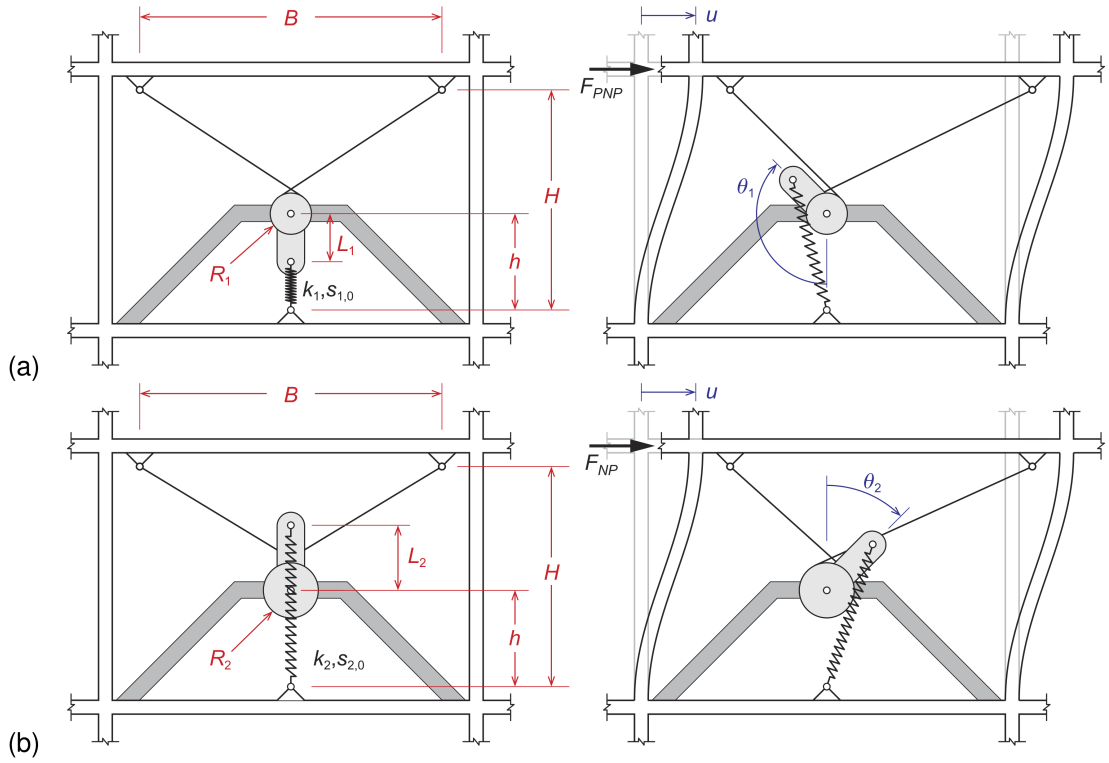



**Figure 2.1:** Geometry and configuration of (a) PNP and (b) NP devices.

negative-positive (NP) stiffness device (Fig. 2.1(b)). The combined resisting force of the SNSD can be expressed as

$$F_{\text{SNSD}}(u) = F_{\text{PNP}}(u) + F_{\text{NP}}(u) \tag{2.1}$$

where $F_{\text{PNP}}$ and $F_{\text{NP}}$ = forces provided by PNP and NP devices, respectively, for a given horizontal deflection $u$ of the structure. To find $F_{\text{PNP}}$ and $F_{\text{NP}}$, consider the geometries of the two devices shown in Fig. 2.1. The devices are driven by independent systems of cables and pulleys that convert translational deflection $u$ to rotations $\theta_1$ and $\theta_2$ ($\circlearrowleft^+$) in the PNP and NP devices, respectively; the relationships $\theta_i(u)$ are discussed below. These rotations in turn stretch and contract springs that are attached at one end to the floor and at the other end to lever arms (of lengths $L_1$ and $L_2$) connected to the pulley. The height from the center of the pulley to the spring attachment point on the floor is $h$ in both devices. In the PNP and NP devices, the lever arm is initially oriented vertically

downward and upward, respectively.

Expressions for the potential energy stored in the PNP and NP springs are given by

$$\mathcal{V}_{\text{PNP}}(u) = \tfrac{1}{2}k_1\left(s_{1,0} - \sqrt{(h - L_1\cos\theta_1)^2 + (-L_1\sin\theta_1)^2}\right)^2 \tag{2.2a}$$

$$\mathcal{V}_{\text{NP}}(u) = \tfrac{1}{2}k_2\left(s_{2,0} - \sqrt{(h + L_2\cos\theta_2)^2 + (L_2\sin\theta_2)^2}\right)^2 \tag{2.2b}$$

where $k_i$ = stiffness of the $i$th spring and $s_{i,0}$ = unstretched length of the $i$th spring. The restoring forces provided by the PNP and NP devices are given by the gradient of the potential energies with respect to the lateral deflection $u$, as follows:

$$F_{\text{PNP}} = \frac{\partial\mathcal{V}_{\text{PNP}}}{\partial u} \equiv \frac{\partial\mathcal{V}_{\text{PNP}}}{\partial\theta_1}\frac{\partial\theta_1}{\partial u} \quad \text{and} \quad F_{\text{NP}} = \frac{\partial\mathcal{V}_{\text{NP}}}{\partial u} \equiv \frac{\partial\mathcal{V}_{\text{NP}}}{\partial\theta_2}\frac{\partial\theta_2}{\partial u} \tag{2.3}$$

where

$$\frac{\partial\mathcal{V}_{\text{PNP}}}{\partial\theta_1} = -k_1 h L_1\sin\theta_1\frac{s_{1,0} - \sqrt{(h - L_1\cos\theta_1)^2 + (-L_1\sin\theta_1)^2}}{\sqrt{(h - L_1\cos\theta_1)^2 + (-L_1\sin\theta_1)^2}} \tag{2.4a}$$

$$\frac{\partial\mathcal{V}_{\text{NP}}}{\partial\theta_2} = k_2 h L_2\sin\theta_2\frac{s_{2,0} - \sqrt{(h + L_2\cos\theta_2)^2 + (L_2\sin\theta_2)^2}}{\sqrt{(h + L_2\cos\theta_2)^2 + (L_2\sin\theta_2)^2}} \tag{2.4b}$$

Evaluation of the derivatives $\partial\theta_i/\partial u$ appearing in Eq. (2.3) requires the cable and pulley kinematics. The cables extend from the ceiling above (with attachment points spaced at $B$), wrapping around and driving the pulleys. The height from the cable attachment points on the ceiling to the spring attachment points on the floor is given by $H$. The lengths of the cables on either side of a pulley are approximated by the distance from the cables' ends (pinned to the ceiling above) to the center of the pulley (i.e., neglecting the radius of the pulley, which is assumed small compared to the geometry $H \times B$ and pulley height $h$):

$$\ell(u) = \sqrt{(H - h)^2 + (B/2 \mp u)^2} \tag{2.5}$$

for the left (−) and right (+) cables. The change in cable length (neglecting axial deformation in the cable), from the undeformed to deformed device configuration, corre-

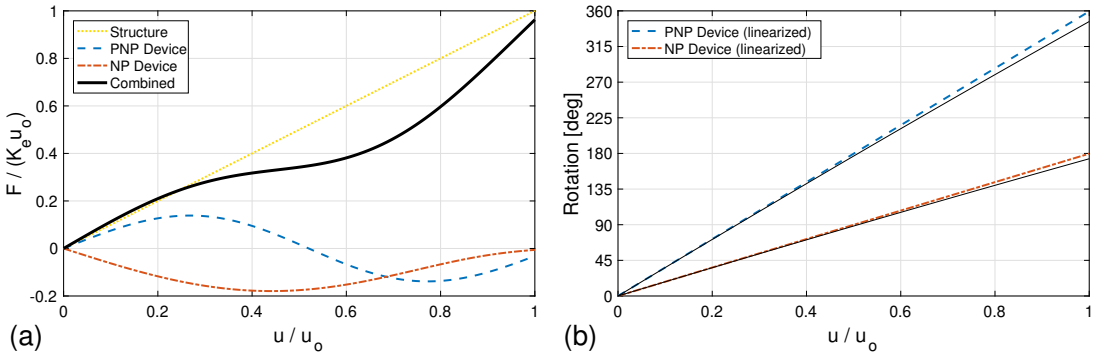



**Figure 2.2:** (a) Theoretical normalized load-deflection relation of an SNSD in parallel with a linear-elastic structure having stiffness $K_e$. (b) The associated rotations in the PNP and NP devices based on Eq. (2.8), with the nonlinear relationships (—) given by Eq. (2.6) for comparison

sponds to a rotation of the pulley given by

$$\theta_i(u) = \frac{\mp[\ell(u) - \ell(0)]}{R_i}, \quad i = 1, 2 \tag{2.6}$$

where $R_i$ = radius of the $i$th pulley. Therefore, the necessary derivatives are as follows:

$$\frac{\partial \theta_i}{\partial u} = \frac{1}{R_i}\frac{\partial \ell}{\partial u} \equiv \frac{1}{R_i}\frac{B/2 \mp u}{\sqrt{(H-h)^2 + (B/2 \mp u)^2}} \tag{2.7}$$

Note that $\partial \ell / \partial u$ is different (in magnitude) for the left and right cables, except for at $u = 0$. For small deflections, the following linearized expression can be assumed:

$$\frac{\partial \theta_i}{\partial u} \approx \left.\frac{\partial \theta_i}{\partial u}\right|_{u=0} = \frac{1}{R_i}\frac{B/2}{\sqrt{(H-h)^2 + (B/2)^2}} \tag{2.8}$$

The second fraction on the right hand side of the equation is recognized to be the cosine of the angle the cable makes with the ceiling.

Having established the geometric relationships that relate the structure's motion $u$ to the SNSD's restoring forces $F_{\text{PNP}}$ and $F_{\text{NP}}$, a theoretical load-deflection relation can be created. Representative load-deflection and rotation-deflection relations are shown in Fig. 2.2, where the reference deflection $u_o$ corresponds to one revolution in the PNP device based on Eq. (2.8) [i.e., $2\pi = (\partial\theta_1/\partial u)|_{u=0} \times u_o$]. Shown in Fig. 2.2(a), the combined load-deflection relation demonstrates little modification to the structure's linear

stiffness at small deflections since the PNP and NP devices largely cancel each other's effects. At larger deflections, the relation exhibits clear apparent weakening as the PNP device transitions to providing negative stiffness. The PNP device's contribution to negative stiffness helps to reduce the size of springs required in both devices. This is a benefit over the ANSS system of Pasala et al. (2013) and is similar to the relationship between the N-P and N-N discs in Walsh et al. (2018). This transition from the linear structure behavior to the apparent weakening behavior is smooth as the PNP lever arm crests its rotation and begins moving downward. As the structure continues to deflect, both the PNP and NP devices smoothly begin to stiffen, mimicking post-yield stiffening in the system. The combined load-deflection relation shown in Fig. 2.2(a) represents an SNSD with zero-negative-positive (ZNP) stiffness per the nomenclature of Walsh et al. (2018); a ZNP-type SNSD is considered in the experimental portion of this work. Other load-deflection relations, e.g., zero-negative-zero (ZNZ) stiffness (Walsh et al., 2018), can also be achieved through proper tuning of the PNP and NP devices, which is described in Section 2.5.

Fig. 2.2(b) shows the associated rotations $\theta_1$ and $\theta_2$ in the PNP and NP devices, respectively, corresponding to the load-deflection relations in Fig. 2.2(a). The PNP device completes one full revolution, whereas the NP device completes a half of a revolution. For comparison, the nonlinear relationship given by Eq. (2.6) and the linear relationship based on Eq. (2.8) [i.e., $\theta \approx (\partial\theta_i/\partial u)|_{u=0} \times u$] are both shown. For the geometry considered, the linearization is sufficiently accurate.

### 2.2.1 A Note on Scalability

From the preceding development, a few important scaling laws can be found. Namely, if the device geometry ($H$, $B$, $h$, $L_i$, and $s_{i,0}$) is scaled by a constant factor $\gamma_{\text{geom}}$ and the deflection $u$ is scaled by a constant factor $\gamma_{\text{defl}}$ (e.g., if a smaller deflection operating range is desired), then the stiffnesses $k_i$ and radii $R_i$ would need to be scaled respectively

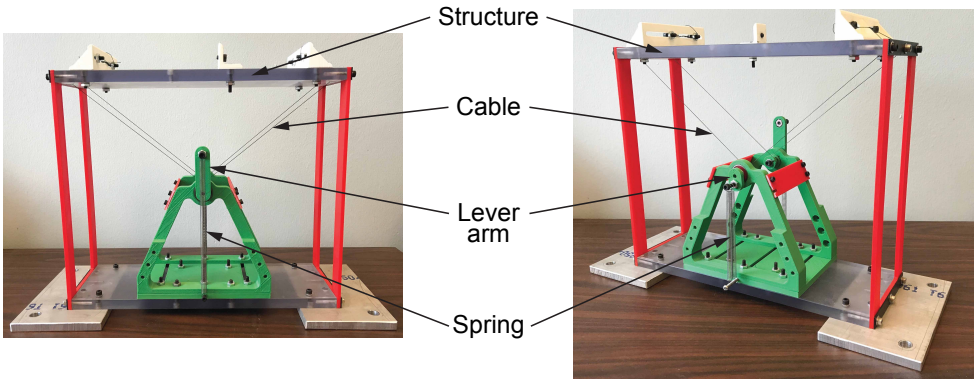



**Figure 2.3:** Experimental prototype of an SNSD: Left, the NP device in the foreground; Right, the PNP device in the foreground.

by $\gamma_{\text{geom}}^{-2}\gamma_{\text{defl}}$ and $\gamma_{\text{defl}}$ to maintain the desired load-deflection relation. These scaling laws provide a redundancy in the selection of the SNSD parameters to achieve a desired load-deflection relation $F_{\text{SNSD}}(u)$, which is beneficial in the design of such a system.

## 2.3 Experimental Prototype

An SNSD was fabricated for installation within a bench-scale, one-story experimental structure, as shown in Fig. 2.3. The experimental structure was approximately 270 mm tall, 300 mm wide, and 108 mm deep (10 in. by 12 in. by 4.25 in.), and made of two stiff polycarbonate floors and four 3D-printed columns attached with rigid moment connections. The columns were flexible and capable of undergoing large drifts (greater than 10%) within the elastic range (Porter et al., 2019). Braided line was used for the cables to transfer the translational motion of the top floor of the structure to the SNSD. The cables were wrapped around the pulleys of the devices and secured to the top floor so that the proper orientation of the lever arms was maintained when at rest ($u = 0$). The springs were attached to the lever arms and then stretched to the base of the device.

Note that two cables were used for each device, as opposed to using a single continuous cable wrapping around the pulley; this was done to prevent the cable from slipping due to the differential lengthening of the cables on either side of the pulleys (cf. Eqs. (2.5)–(2.7)). As a result, only one of the cables was engaged at a given deflection, de-

pending on what stage the respective device was in; i.e., for $u > 0$, the right cable for a device providing positive stiffness and the left cable for a device providing negative stiffness. In this configuration, force was transferred from the lever arm shaft to the cable by the connection of the cable to the pulley rather than by friction on the pulley.

The length of the lever arms, radii of the pulleys, and properties of the springs were determined using a mathematical model of the device in MATHEMATICA. While the experimental structure could withstand larger deflections, a maximum desired deflection was set at 25.4 mm (1 in.) for the design of this SNSD. For designing the parameters of the device, two criteria were sought. The first criterion was for the SNSD to have zero stiffness at $u = 0$, so it would not modify the structure's linear elastic stiffness $K_e$ at small deflections. The second criterion was to achieve the maximum negative stiffness in the SNSD at half of the maximum deflection $u_o$; this maximum negative stiffness was determined as a percentage of the stiffness of the elastic structure. These criteria can be expressed mathematically as follows:

$$\text{Criterion 1:} \quad K_{\text{SNSD}}\Big|_{u=0} = 0 \tag{2.9a}$$

$$\text{Criterion 2:} \quad K_{\text{SNSD}}\Big|_{u=u_o/2} = (\tilde{\alpha} - 1)K_e \tag{2.9b}$$

where $K_{\text{SNSD}} \equiv \partial F_{\text{SNSD}}/\partial u$ = the tangential stiffness of the SNSD and $\tilde{\alpha}$ = the apparent post-yield stiffness ratio.

The dimensions of the structure and the devices are shown in Fig. 2.4. For clarity, only one device is shown, and the dimensions and properties of the SNSD components are tabulated in Table 2.1. 3D printing was used to produce the frames, arms, and pulleys, and springs were selected from a supplier. The spring stiffnesses in Table 2.1 were determined experimentally by hanging masses and measuring the resulting deflection. The PNP and NP devices were fabricated and installed in the structure opposite one another (see Fig. 2.3). This experimental prototype was subjected to static and dynamic

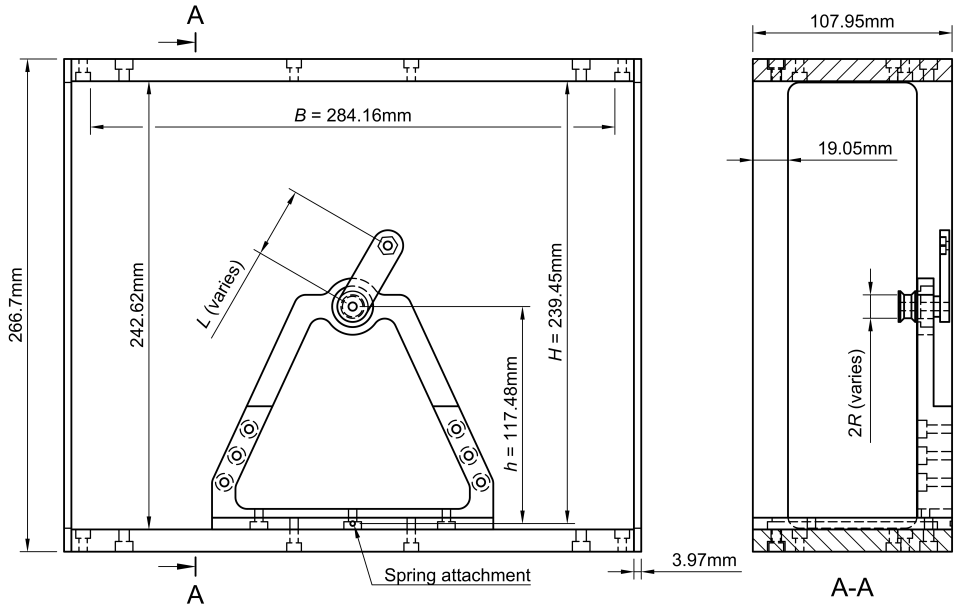



**Figure 2.4:** Dimensioned drawings of experimental prototype (with only one device shown).

tests in order to characterize its behavior and performance, which is described in the next section.

## 2.4 Experimental Results

### 2.4.1 Characterization Tests

The load-deflection behavior of the combined structure-SNSD system was first characterized by static tests. The device was fixed to a table and a universal testing machine was used to apply a lateral load at a constant displacement rate of 50 mm/s to a maximum deflection of 25 mm. This test was performed for each combination of spring at-

**Table 2.1:** Experimental SNSD dimensions and parameters.

| PNP Device | | NP Device | |
|---|---|---|---|
| Variable | Value | Variable | Value |
| $R_1$ [mm] | 3.18 | $R_2$ [mm] | 6.35 |
| $L_1$ [mm] | 8.26 | $L_2$ [mm] | 44.5 |
| $s_{1,0}$ [mm] | 47.6 | $s_{2,0}$ [mm] | 63.5 |
| $k_1$ [N/m] | 21.8 | $k_2$ [N/m] | 9.14 |

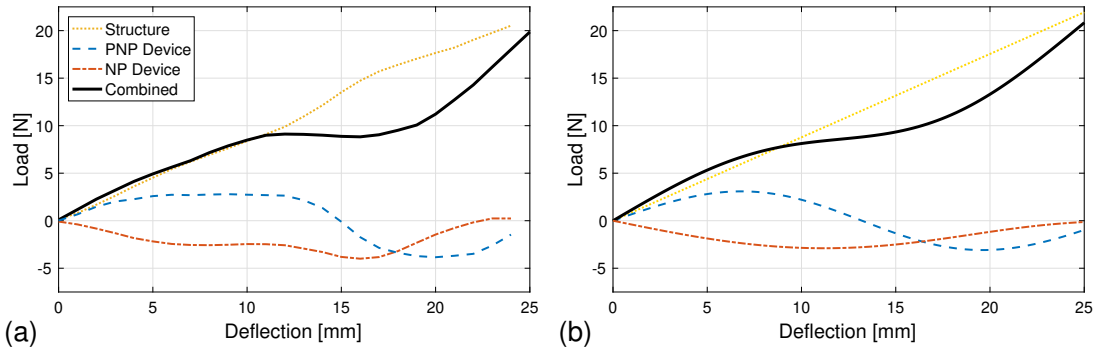



**Figure 2.5:** (a) Experimental and (b) theoretical load-deflection relations of the elastic structure, SNSD component devices, and combined structure-SNSD system.

tachments: all springs attached, only the NP spring, only the PNP spring, and no springs attached. The setup was then rotated 180° to apply the lateral load in the opposite direction. The results from these tests are shown in Fig. 2.5(a), where the lines represent the average of six tests (three in each direction). The case of no springs attached is denoted as "Structure," and "Combined" is the case of all springs attached. The experimental PNP and NP curves were determined by testing the system with the respective springs attached and then subtracting the structure's stiffness from those results.

For comparison, the theoretical load-deflection relation from Fig. 2.2(a) without normalization is given in Fig. 2.5(b). Good agreement can be seen between the shapes of the experimental and theoretical curves, clearly demonstrating that apparent weakening was achieved. The combined structure-SNSD system curve closely follows the linear structure at low deflections. Initially, a slight stiffening effect can be seen, but from 5 to 10 mm, the stiffnesses are almost exactly the same. The structure softens smoothly yet quickly to exhibit apparent weakening after 11 mm of deflection. A gradual stiffening begins at 17 mm of deflection and increases as the maximum deflection is reached.

The cause of the SNSD effect can be clearly seen in how the NP and PNP devices performed. At small deflections, the PNP device had a slightly greater positive stiffness than the magnitude of the NP device's negative stiffness. This resulted in a slight increase in the combined system stiffness over the first 5 mm of deflection. Between 5 and

10 mm, the loads of both devices plateaued at loads equal in magnitude, which slightly deviates from the expected theoretical results (Fig. 2.5(b)); however, it still provided the desired cancelling effect for these small deflections. These deviations are believed to be related to flexibilities in the cables and 3D-printed parts that are not represented in the theoretical model. The NP device develops some additional negative stiffness around 11 mm before reaching a minimum load and turning positive again at 17 mm. This initiates the apparent weakening in the combined system, and just as the NP device transitions from negative to positive stiffness, the PNP device reaches a maximum negative stiffness, which continues the apparent weakening region of the combined system until 17 mm. As the PNP device transitions to positive stiffness, the NP device provides positive stiffness. For the last few millimeters of deflection, both devices add positive stiffness to the combined system, resulting in the steep positive slope from 21 to 25 mm.

The nominally linear structure displayed some slight nonlinearities, especially as the maximum deflection was approached. Even when the springs were not attached, the cables remained wound around the pulleys, so the flexibility of the components of the SNSD and the way the cables spooled around the pulleys could have contributed to this. Additionally, these tests pushed the structure to extreme drifts (25 mm or approximately 10% of the structure's height), which could have introduced further geometric nonlinearities. Some uncertainty also exists in the precision of the 3D-printed parts.

### 2.4.2 Harmonic Excitation

The experimental system was connected to a shake table for dynamic characterization. This experimental setup of the combined structure-SNSD system on the shake table is depicted in Fig. 2.6. The acceleration of the table and of the top floor of the structure (hereafter referred to as "table acceleration" and "structure acceleration," respectively) were measured by rigidly attached piezoelectric accelerometers (393B04, PCB, Depew, NY). The system was subjected to sine sweeps through frequencies from 2 to 10 Hz. A

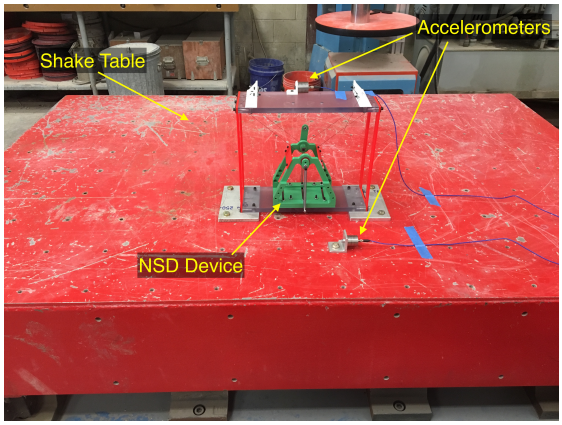



**Figure 2.6:** Experimental system installed on shake table with connected accelerometers.

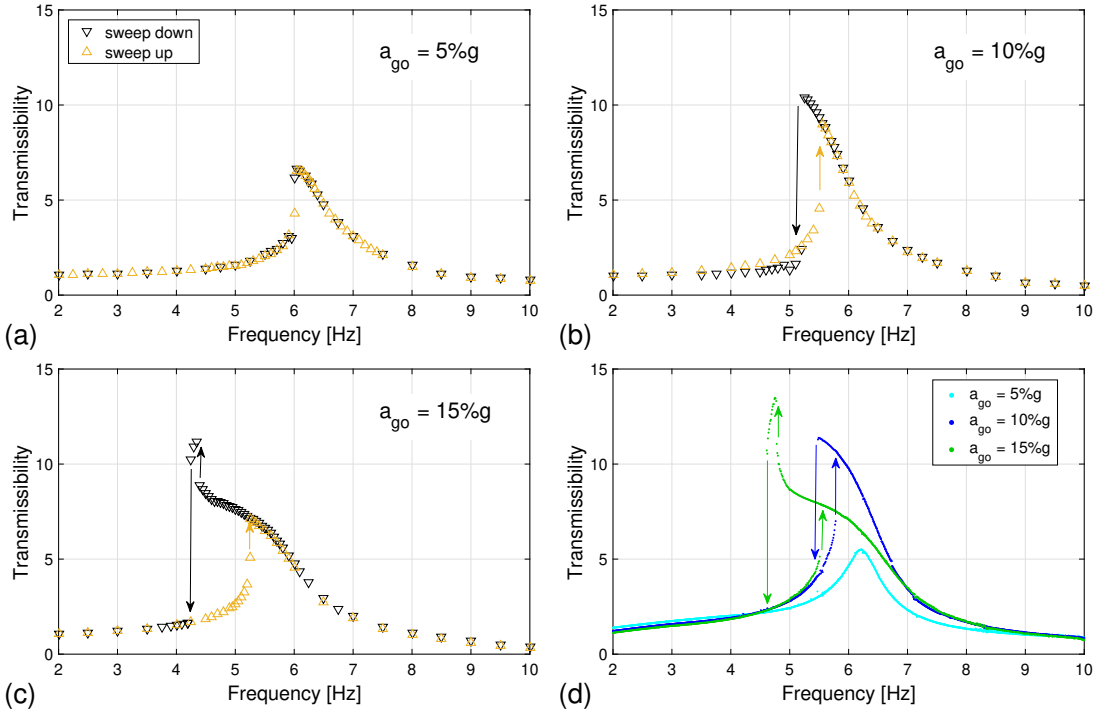



**Figure 2.7:** Transmissibility under harmonic excitation of varying peak ground acceleration, $a_{go}$: (a–c) experiments for $a_{go}$ = (a) 5, (b) 10, and (c) 15%$g$ and (d) theory.

sweep increasing and a sweep decreasing in frequency ("sweep up" and "sweep down") were performed for varying table acceleration amplitudes (5, 10, and 15%$g$) in order to capture the nonlinear behavior of the device. The results of these tests are summarized in the transmissibility plots (peak structure acceleration to peak table acceleration) of Fig. 2.7.

In a nonlinear system, the frequency response is distinctly different than that of a linear system. Frequency shifting due to a change in stiffness of the system allows for more than one steady-state response at some frequencies. Depending on the amplitude of the ground excitation and the preceding excitation (i.e., hysteresis), the system may "jump" to a higher response from a lower one, or conversely "fall" from a higher to a lower. These jumps are indicated in Fig. 2.7 by arrows. Softening behavior is apparent in all the experimental sweeps, characterized by the transmissibility curve bending to the left (lower frequencies). On the sweeps up, the response increases with an increase in frequency as a typical linear system would approaching resonance. When the system deflects enough to begin to engage the softening effects of the SNSD, the response shows an abrupt jump up in transmissibility. On the sweeps down, the system—already excited enough for the softening effects to be present—continues to exhibit a large response until it eventually falls when the higher branch of the response vanishes. This hysteretic effect is clearly observed for the case of a peak table acceleration of $10\%g$ (Fig. 2.7(b)). Interesting to note in the $15\%g$ plot (Fig. 2.7(c)) is that the system jumped up to yet another higher response. This third stable branch is present because of the stiffening effect at large deflections (20–25 mm; see Fig.2.5)

The governing equation of motion for the experimental structure-SNSD system can be represented as

$$m\ddot{u}(t) + c\dot{u}(t) + F_{\mathrm{f}}\,\mathrm{sgn}[\dot{u}(t)] + F_{\mathrm{SNSD}}(u) + K_e u(t) = -m\ddot{u}_{\mathrm{g}}(t) \tag{2.10}$$

where $m$ and $c$ = the structure's mass and damping coefficient, respectively; $F_{\mathrm{f}}$ = friction force amplitude; and $\ddot{u}_{\mathrm{g}}(t)$ = ground acceleration. Note that friction, which may be attributed to slipping of the cables on the pulleys, was incorporated into the numerical model to better match the experimental results, in particular for the lowest peak ground acceleration ($a_{go} = 5\%g$, Fig. 2.7(a)), for which friction had the greatest influence. The

friction force [0.228 N (0.0512 lb)] and damping coefficient [1.28 N·s/m ($7.3 \times 10^{-3}$ lb·s/in.), which is 2.5% of critical damping for the structure] used in the numerical model were fit to most closely resemble the experimental results (Figs. 2.7(a–c)). The mass $m$ and elastic stiffness $K_e$ were determined to be 0.748 kg ($4.27 \times 10^{-3}$ lb·s$^2$/in.) and 877 N/m (5.01 lb/in.), respectively. The numerical model of the structure-SNSD system was subjected to sine sweeps at 5, 10, and 15%$g$ peak ground acceleration. The model used the as-built parameters and properties of the device and the structure (Table 2.1). The resulting frequency response curve, shown in Fig. 2.7(d), showed good agreement with the experimental results. The softening effect is exhibited by the bending over of the response curves and the jumping and falling of the response. The tertiary stable branch due to the stiffening effect (cf. previous paragraph) is also present in the theoretical results (Fig. 2.7(d)), and the system jumps to a higher response for $a_{go} = 15\%g$ on the sweep down.

### 2.4.3 White Noise Excitation

White noise excitation was also used to understand the structure's response to excitation similar to that of an earthquake. To study the response of the system under different input energy levels, bandpass (1–20 Hz) filtered white noise was linearly scaled to increasing peak ground accelerations and applied to the experimental system. An example of the white noise excitation time history is shown in Fig. 2.8(a), and the system's response to this excitation is shown in Fig. 2.8(b). The results of the white noise tests are summarized in Fig. 2.9. A softening effect can be observed in the system's response beginning around 40%$g$, continuing until just below 80%$g$. Above 80%$g$, the system shows a stiffening response with an increase in acceleration.

The numerical model was subjected to the same white noise excitations, and these results are also presented in Fig. 2.9. The simulation shows a similar response to the experiment, especially at the lower amplitudes below 70%$g$. Above this, the experi-

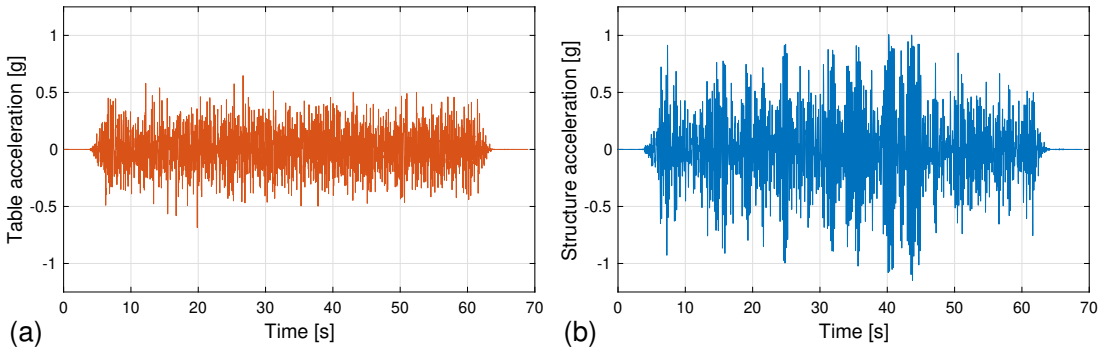



**Figure 2.8:** (a) Time history of the white noise excitation to which the experimental structure-SNSD system was subjected, and (b) response of the system.

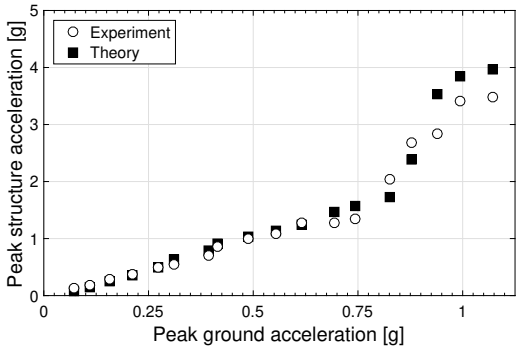



**Figure 2.9:** Peak structure acceleration under white noise excitation of varying intensity.

ments and theory diverge slightly, with the simulations predicting higher accelerations, but overall reasonable correspondence between the experiments and theory is observed, especially with regard to softening/stiffening behavior.

## 2.5 Simulated Earthquake Response

### 2.5.1 Simulated Structure and Device Parameters

To investigate the performance of the SNSD in a realistic building under an earthquake, a model was developed based on the one-third scale experimental structure of Pasala et al. (2014). This structure is a three-story experimental frame with cross braces on the top two stories. It was modeled as a single degree-of-freedom (SDOF) structure with a floor weight of 114.7 kN (25.8 kips), elastic stiffness $K_e$ of 1909 kN/m (10.9 kip/in.), and an inherent damping ratio of 1.6%. Inelastic effects were incorporated into

the simulated system using the Bouc-Wen model with a post-yield stiffness of $\alpha = 1/6$. The structure's yield deflection was $u_y = 2.79$ cm (1.1 in.). The governing equation of motion for this SDOF system was

$$m\ddot{u}(t) + c\dot{u}(t) + F_{\text{SNSD}}(u) + \alpha K_e u(t) + (1-\alpha)K_e z(t) = -m\ddot{u}_g(t) \tag{2.11}$$

where

$$\dot{z}(t) = A\dot{u}(t) - \beta|\dot{u}(t)||z(t)|^{n-1}z(t) - \gamma\dot{u}(t)|z(t)|^n \tag{2.12}$$

and $A = 1.0$, $\beta = \gamma = 0.5$, and $n = 20$ (Walsh et al., 2018). Pasala et al. (2013) reported that a viscous damper was added to limit excessive deflections, which resulted in an effective damping ratio of 22.1%, which is included in some cases for comparison.

SNSDs were configured for modeling in this structure by developing two desired load-deflection relations that follow the zero-negative-positive stiffness (ZNP) and zero-negative-zero stiffness (ZNZ) configurations proposed by Walsh et al. (2018). For each configuration, three different relations —the ideal relation ("Ideal"), the modified relation used as the target for optimization ("Target"), and the fitted relation found through optimization ("Fitted")—are presented in Fig. 2.10. The ideal curve is based on values taken from Pasala et al. (2014), with yield deflection $u_y = 2.79$ cm (1.1 in.), apparent yield deflection $u'_y = 0.25u_y = 0.699$ cm (0.275 in.), and effective stiffness of the SNSD after apparent yielding of $K_{\text{SNSD}} = -K_e$. When this relation was written into a Levenberg–Marquardt (Levenberg, 1944) algorithm in MATLAB (Gavin, 2017), there were convergence issues caused by trying to fit a smooth transition from zero to negative stiffness in such a small deflection window ($u < 0.25u_y$); Gibbs phenomenon-like behavior was also observed, resulting in excessively large negative stiffnesses. To accommodate these issues, $u_y$ and $u'_y$ were adjusted and the target stiffness of the device was reduced. These adjusted values—$u_y = 3.18$ cm (1.25 in.), $u'_y = 0.4u_y = 1.27$ cm (0.3125 in.), and $K_{\text{eff}} = 0.82K_e$—are represented by the target relation, which is ulti-

mately what was fit to in the parameter optimization. The optimization algorithm was run multiple times for both configurations from randomly seeded initial parameter values, and the global optima of the parameters were selected. The optimized parameters of the two different devices are tabulated in Table 2.2. The resulting fitted relations are acceptable approximations to the ideal relations. The negative stiffness (slope in Fig. 2.10) produced by the fitted relations matches the negative stiffness of the ideal relation (and that of the structure), and both fitted relations smoothly transition from zero to negative to their final stiffness successfully.

The relations are designed for an operable range up to $2u_y$. Deflections in excess of this are expected to cause significant changes to the stability and dynamics of the structure and device that are not captured in this model. Performance outside this range of $\pm 2u_y$ is therefore not considered as representative of the performance of these devices.

In order to make the spring sizes more realistic, $h$, the distance from the center of the pulley to the spring attachment point, was reduced. This in turn limited the maximum lengths of the springs and lever arms. This geometric reduction resulted in a quadratic increase of the spring stiffnesses used (see Section 2.2.1).

### 2.5.2 Ground Motions used in Numerical Simulations

The mathematical model of the SNSD-structure systems were subjected to a suite of historic and synthetic ground motions (GMs). The historic GMs, which give a range of inelastic response (Walsh et al., 2018), are summarized in Table 2.3, and the first thirty

**Table 2.2:** Dimensions and parameters of the fitted SNSDs.

| NP Device | | | PNP Device | | |
|---|---|---|---|---|---|
| Variable | ZNP Value | ZNZ Value | Variable | ZNP Value | ZNZ Value |
| $R_1$ [cm] | 2.04 | 3.91 | $R_2$ [cm] | 0.452 | 0.466 |
| $L_1$ [cm] | 36.8 | 38.1 | $L_2$ [cm] | 6.21 | 8.15 |
| $s_{1,0}$ [cm] | 38.1 | 2.54 | $s_{2,0}$ [cm] | 35.6 | 32.0 |
| $k_1$ [N/cm] | 75.1 | 137 | $k_2$ [N/cm] | 67.3 | 37.9 |

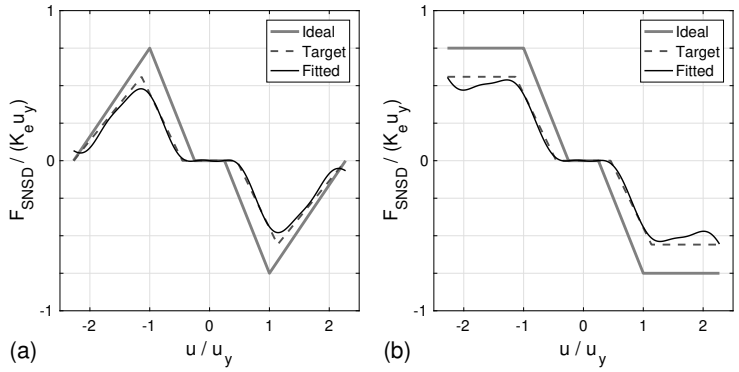



**Figure 2.10:** Comparison of ideal, target, and fitted load-deflection relations used in the SNSD simulations: (a) ZNP and (b) ZNZ configurations

seconds of the time histories are shown in Fig. 2.11. The synthetic GMs were generated using the statistical models from Gavin and Dickinson (2011). These synthetic GMs are characteristic of the suites of GM records developed for the SAC Steel Project, representing GMs with an exceedance probability of 10% or 2% in 50 years for Los Angeles or Seattle for a site class D (firm soil), in addition to near-fault GMs near Los Angeles. Ten synthetic GMs were generated for each of the five data sets: Los Angeles, 10% and 2% in 50 years ("la10in50" and "la2in50"); Seattle, 10% and 2% in 50 years ("se10in50" and "se2in50"); and near-fault ("nrfault"). Only one component of each of the bidirectional synthesized GMs was used.

The 5%-damped acceleration response spectra for the historic and synthetic GMs are presented in Fig. 2.12. For the synthetic GMs, the individual spectra are presented, as well as their mean ($\mu$) and mean plus/minus one standard deviation ($\mu \pm \sigma$). Based on similitude for the third scale structure, the records were scaled in time by a factor of $3^{-1/2}$. The GM records and spectra shown in Figs. 2.11 and 2.12 are unscaled.

### 2.5.3 Simulation Results

The performance of the ZNP and ZNZ SNSDs is evaluated by comparing the response for the following cases: (1) the base structure (BS); (2) the base structure with the supplemental viscous damper (BS+VD); and (3) the base structure, viscous damper,

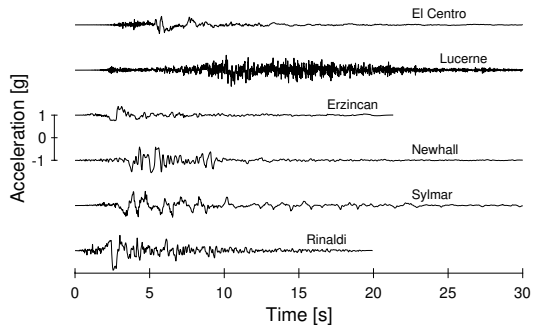



**Figure 2.11:** Historic ground motion time histories (unscaled).

and SNSD assembly (BS+VD+ZNP and BS+VD+ZNZ). Each case was subjected to all GMs. To measure the performance of the devices, the modified performance indices of Pasala et al. (2013) were adopted. These are defined in Table 2.4, where $V(t)$ is base shear in the structure and $F_R(t)$ is the total restoring force in the structure-SNSD system given by

$$F_R(t) = F_{\text{SNSD}}(u) + \alpha K_e u(t) + (1 - \alpha) K_e z(t) \tag{2.13}$$

It is worth noting that both $J_1$ and $J_4$ are dependent on the deflection of the structure, while $J_2$ and $J_3$ are dependent on acceleration.

The performance indices obtained for the simulations are presented in Tables 2.5 and 2.6 for the historic and synthetic GMs, respectively. Immediately apparent from the simulation results is the reduction in deflections ($J_1$) in all cases due to the additional damping (BS+VD) when compared to the base structure (BS). The addition

**Table 2.3:** Summary of historic earthquake motions (unscaled).

| Earthquake event / Station / Component | PGA ($g$) | PGV (cm/s) | PGD (cm) |
|---|---|---|---|
| 1992 Erzincan, Turkey / Erzincan / NS | 0.387 | 107 | 32.0 |
| 1994 Northridge / Rinaldi Receiving Sta. / 228 | 0.874 | 148 | 41.9 |
| 1994 Northridge / Sylmar - Converter Sta. / 52 | 0.623 | 116 | 39.4 |
| 1994 Northridge / Newhall - Fire Sta. / 360 | 0.590 | 96.5 | 34.3 |
| 1992 Landers / Lucerne / 260 | 0.725 | 133 | 114 |
| 1979 Imperial Valley / El Centro Array #5 / 230 | 0.383 | 96.9 | 75.2 |

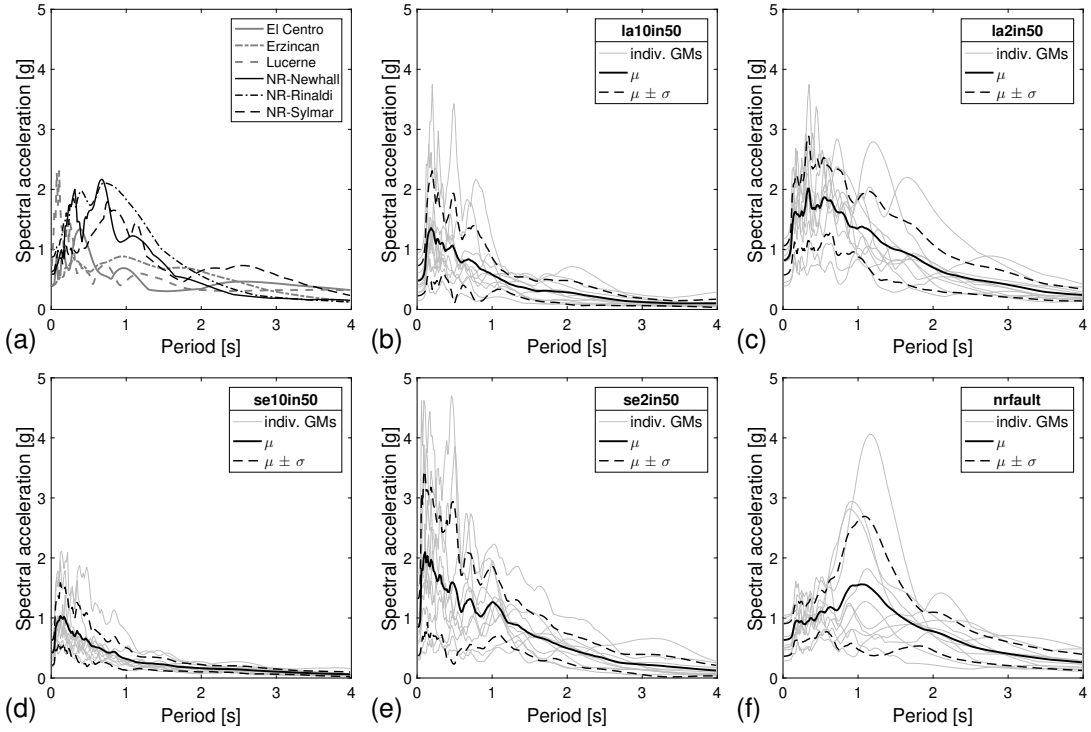



**Figure 2.12:** Linear elastic response spectra (5% damped) for (a) historic and (b–f) synthetic ground motions (GMs)

of damping also reduced accelerations ($J_2$) in about half of the cases. Therefore, the BS+VD results—instead of the BS results—are used to benchmark the performance of the SNSDs (BS+VD+ZNP and BS+VD+ZNZ).

For the historical GMs (Table 2.5), the SNSDs performed as expected, reducing accelerations and increasing deflections in almost all cases. At deflections less than $u_y$ ($J_1 < 1$), both configurations (BS+VD+ZNP and BS+VD+ZNZ) had similar responses, since the load-deflection relations are not substantially different until after yielding has

**Table 2.4:** Definitions of the performance indices.

| Performance index | Description | Formula |
|---|---|---|
| $J_1$ | Normalized peak deflection | $\max_t \lvert u(t)\rvert / u_y$ |
| $J_2$ | Normalized peak acceleration | $\max_t \lvert \ddot{u}_g(t) + \ddot{u}(t)\rvert / \max_t \lvert \ddot{u}_g(t)\rvert$ |
| $J_3$ | Normalized peak base shear | $\max_t \lvert V(t)\rvert / (K_e u_y)$ |
| $J_4$ | Normalized peak restoring force | $\max_t \lvert F_R(t)\rvert / (K_e u_y)$ |

**Table 2.5:** Performance indices from the historic GM simulations

| Performance index | System | El Centro | Lucerne | Erzincan | Newhall | Sylmar | Rinaldi |
|---|---|---|---|---|---|---|---|
| $J_1$ | BS | 1.690 | 1.287 | 2.592 | 2.995 | 3.150 | 6.170 |
| | BS+VD | 0.831 | 0.913 | 1.334 | 1.705 | 2.004 | 3.364 |
| | BS+VD+ZNP | 1.078 | 1.134 | 1.816 | 1.902 | 2.098 | 3.051 |
| | BS+VD+ZNZ | 1.073 | 1.129 | 2.016 | 1.995 | 3.179 | 3.901 |
| $J_2$ | BS | 1.355 | 0.674 | 1.524 | 1.054 | 1.017 | 0.995 |
| | BS+VD | 1.063 | 0.630 | 1.485 | 1.266 | 1.077 | 1.042 |
| | BS+VD+ZNP | 0.876 | 0.470 | 1.223 | 1.144 | 1.018 | 1.007 |
| | BS+VD+ZNZ | 0.882 | 0.471 | 1.102 | 1.063 | 0.993 | 0.838 |
| $J_3$ | BS | 1.117 | 1.051 | 1.268 | 1.340 | 1.363 | 1.871 |
| | BS+VD | 0.876 | 0.984 | 1.236 | 1.609 | 1.444 | 1.960 |
| | BS+VD+ZNP | 0.722 | 0.734 | 1.018 | 1.453 | 1.364 | 1.895 |
| | BS+VD+ZNZ | 0.728 | 0.735 | 0.917 | 1.351 | 1.331 | 1.576 |
| $J_4$ | BS | 1.115 | 1.048 | 1.265 | 1.333 | 1.358 | 1.862 |
| | BS+VD | 0.831 | 0.907 | 1.056 | 1.117 | 1.167 | 1.394 |
| | BS+VD+ZNP | 1.006 | 1.020 | 1.136 | 1.150 | 1.183 | 1.342 |
| | BS+VD+ZNZ | 1.004 | 1.019 | 1.169 | 1.166 | 1.363 | 1.483 |

**Table 2.6:** Performance indices from the synthetic GM simulations

| Performance index | System | la10in50 | la2in50 | se10in50 | se2in50 | nrfault |
|---|---|---|---|---|---|---|
| $J_1$ | BS | 1.482 | 3.793 | 1.125 | 2.379 | 4.380 |
| | BS+VD | 0.795 | 2.019 | 0.436 | 1.339 | 2.229 |
| | BS+VD+ZNP | 0.860 | 2.142 | 0.449 | 1.698 | 2.437 |
| | BS+VD+ZNZ | 0.900 | 2.854 | 0.451 | 2.158 | 2.950 |
| $J_2$ | BS | 1.106 | 0.878 | 1.211 | 0.777 | 1.201 |
| | BS+VD | 0.831 | 0.917 | 0.559 | 0.786 | 1.105 |
| | BS+VD+ZNP | 0.749 | 0.846 | 0.546 | 0.709 | 1.094 |
| | BS+VD+ZNZ | 0.743 | 0.813 | 0.545 | 0.686 | 0.948 |
| $J_3$ | BS | 1.003 | 1.471 | 0.957 | 1.196 | 1.565 |
| | BS+VD | 0.827 | 1.575 | 0.490 | 1.249 | 1.472 |
| | BS+VD+ZNP | 0.735 | 1.454 | 0.465 | 1.152 | 1.504 |
| | BS+VD+ZNZ | 0.723 | 1.387 | 0.464 | 1.091 | 1.268 |
| $J_4$ | BS | 1.000 | 1.465 | 0.955 | 1.192 | 1.559 |
| | BS+VD | 0.695 | 1.156 | 0.431 | 0.995 | 1.152 |
| | BS+VD+ZNP | 0.725 | 1.189 | 0.433 | 1.063 | 1.193 |
| | BS+VD+ZNZ | 0.732 | 1.308 | 0.434 | 1.141 | 1.278 |

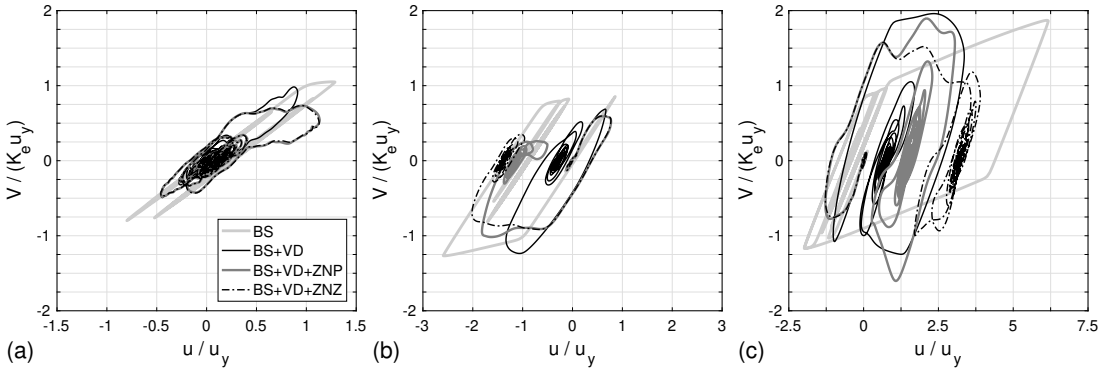



**Figure 2.13:** Normalized load-deflection responses for (a) Lucerne, (b) Erzincan, and (c) Rinaldi

occurred (see Fig. 2.10). This is shown in the results from the Lucerne GM, presented in Fig. 2.13(a), where the systems with ZNP and ZNZ devices track almost identically with one another resulting in reduced base shears and larger deflections than the BS+VD system. For more intense GMs, such as Erzincan (Fig. 2.13(b)), the difference in the ZNP and ZNZ responses is more pronounced. Both SNSD systems produced smaller peak base shears than the BS and BS+VD systems, and the BS+VD+ZNZ response clearly illustrates the further increase in deflection and reduction of forces without the stiffening in the ZNP device. As a consequence, the resulting residual deflections for the ZNP and ZNZ systems ($1.16u_y$ and $1.39u_y$, respectively) were larger than the BS+VD system ($0.28u_y$), which was observed for most of the historical GMs. The only case in which an SNSD decreased peak deflections was for the ZNP device under the Rinaldi GM (Fig. 2.13(c)), but this was occurring at over three times the structure's yield deflection, well outside the intended operating range of the SNSDs (Fig. 2.10). While the BS+VD+ZNP had a smaller peak deflection than the BS+VD, the response does show reduced peak forces and increased residual deflections. The increased deflections resulting from the addition of SNSDs remained less than the deflections of the BS for all cases except the ZNZ SNSD under the Sylmar GM.

Fig. 2.14 shows the average changes in performance due to the addition of a SNSD. In general, peak deflections ($J_1$) and restoring forces ($J_4$) are increased due to the SNSD,

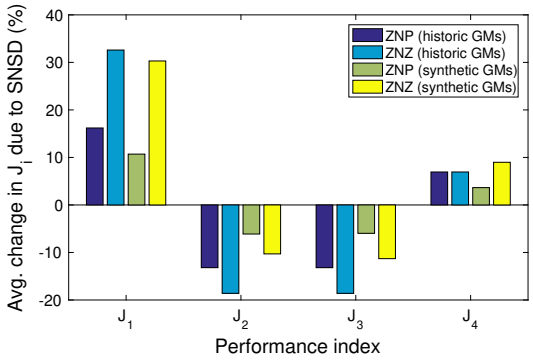



**Figure 2.14:** Average change in performance index $J_i$ (Table 2.4) due to the addition of an SNSD, using the performance of a system without an SNSD (BS+VD) to benchmark those with SNSDs (BS+VD+ZNP and BS+VD+ZNZ).

while peak accelerations ($J_2$) and base shear ($J_3$) are decreased. Simulations were also run using the target load-deflection relations used for the optimization and design of the fitted devices (see Fig. 2.10), and the results (not shown) matched closely for both the historic and synthetic GMs.

## 2.6 Summary

This chapter presented an investigation of a novel smooth negative stiffness device (SNSD) for the seismic mitigation of structures through apparent weakening. The load-deflection relation of the SNSD was developed, and an experimental prototype was fabricated for testing. This prototype was subjected to static, harmonic, and white noise loading to characterize the effect of the SNSD. The static tests proved that the desired load-deflection relation was indeed obtained in the prototype. The harmonic loading showed the highly nonlinear behavior of the structure-SNSD system under dynamic loading, and the white noise testing confirmed the deflection-amplitude dependence of the nonlinear response. Numerical simulations were conducted with two configurations of SNSDs—(1) zero-negative-positive (ZNP) stiffness, similar to the prototype relation, and (2) zero-negative-zero (ZNZ) stiffness—in an inelastic building with supplemental damping, subjected to multiple earthquake ground motions. Both SNSD configu-

rations were optimized to closely match the desired (target) load-deflection relations. These simulation results showed that the SNSDs were effective at reducing peak base shears and limiting peak deflections to less than deflections in the base structure without supplemental damping. When comparing the two configurations of SNSDs, the ZNP configuration increased peak deflections and restoring forces to a lesser degree than the ZNZ configuration, but the ZNP configuration was less effective at limiting peak accelerations and base shears than was the ZNZ configuration. Both configurations closely matched the targeted load-deflection relation in both their respective load-deflection relations and in their peak results. These results show that the proposed SNSD can be effective in producing desired apparent weakening in a structure.

Finally, the relationships between the geometry and the load-deflection relation of the device is readily scalable (see Section 2.2.1). This could be beneficial in the construction of a full-size device for implementation in a structure, because the sizes of the lever arms can be reduced to limit risks of highly stretched springs.

# Chapter 3
# Buckled-Strut Vertical Isolation System

## 3.1 Overview

This chapter presents the development of a buckled-strut vertical isolation system (BSVIS). The system consists of a buckled strut in parallel with linear springs to support and isolate a mass. A schematic of such a BSVIS is pictured in Fig. 3.1. When the strut is loaded laterally, its snap-through behavior results in negative stiffness, and linear springs in parallel with the buckled strut provide a stable region of isolation-level stiffness, which can be tuned to provide proper vertical support of a mass. The development of the load-deflection relation of buckled struts is presented in Section 3.2. The effect of a linear spring is added to the buckled strut to give the load-deflection relation of a BSVIS in Section 3.3. A prototype was developed to characterize the behavior of the BSVIS (Section 3.4), and a proof-of-concept experimental study was conducted through static tests (Section 3.5). Based on the theory and confirmation from the experimental results, a guide for designing a BSVIS is presented (Section 3.6) before the conclusion of this chapter (Section 3.7).

## 3.2 Lateral Load-Deflection Relation of a Buckled Strut

The negative stiffness behavior of the BSVIS is contributed by a laterally loaded buckled strut. The development of the load-deflection relation of such a strut largely follows the development in Harvey and Virgin (2015) of an arch unilaterally constrained. Here,

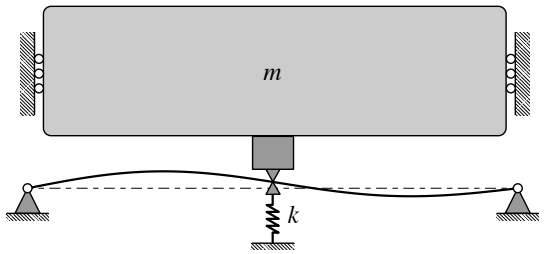



**Figure 3.1:** A schematic of an assembled BSVIS consisting of a buckled strut and a linear spring of stiffness $k$ supporting a payload of mass $m$

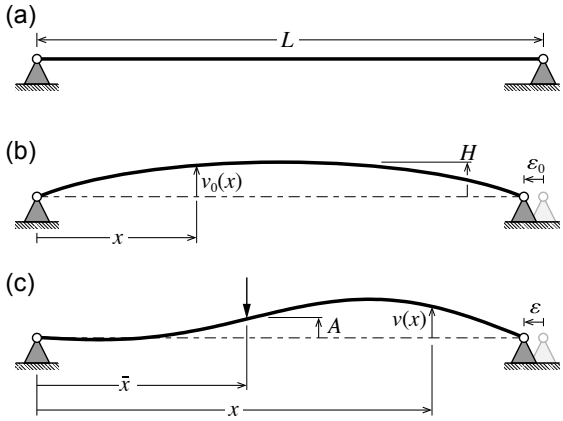



**Figure 3.2:** Geometry and description of a buckled strut: (a) an initially undeformed strut of length $L$; (b) the strut after an end shortening of $\varepsilon = \varepsilon_0$ resulting in the initial deflected shape $v_0(x)$ with lateral rise $H$; (c) the strut when a lateral constraint is enforced such that $v(\bar{x}) = A$.

consider an initially straight, inextensible strut of length $L$, shown in Fig. 3.2(a) as simply-supported. When this is subjected to an initial end shortening of $\varepsilon_0$ (Fig. 3.2(b)), a shallow lateral deflection $v_0(x)$ results, with an associated rise of $H$. Now a lateral constraint is imposed at a point $\bar{x}$ along the length of the strut such that the lateral deflection $v(\bar{x}) = A$ (Fig. 3.2(c)), where $v(x)$ is the general deflected shape and $A$ is the amplitude of the deflected shape at $\bar{x}$. This constraint can be "knife-edge" (Fig. 3.2(c)), where the rotation at $\bar{x}$ is not hindered, or "clamped" (not shown), where a fixed condition is created at $\bar{x}$.

For a general deflected shape $v(x)$, the total elastic strain energy $U$ in the beam can be expressed as (Thompson and Hunt, 1983)

$$U = \frac{1}{2}EI \int_0^L [v''(x)]^2 \left\{1 + [v'(x)]^2 + [v'(x)]^4 + \cdots\right\} dx \approx \frac{1}{2}EI \int_0^L [v''(x)]^2 \, dx \quad (3.1)$$

corresponding to a total end shortening $\varepsilon$ of

$$\varepsilon = \int_0^L \left\{\frac{1}{2}[v'(x)]^2 + \frac{1}{8}[v'(x)]^4 + \frac{1}{16}[v'(x)]^6 + \cdots\right\} dx \approx \frac{1}{2} \int_0^L [v'(x)]^2 \, dx. \quad (3.2)$$

Since the strut buckles to a shallow rise $H$, only the leading terms of both expressions need to be retained as a suitable approximation. Stable equilibria exist when the minima of the strain energy occur, and this minimization is constrained by both the end shortening and the lateral constraint, which can be expressed as follows:

$$\begin{cases} \min\limits_{v(x)} & U = \dfrac{1}{2}EI \displaystyle\int_0^L [v''(x)]^2 \, dx \\ \text{subject to} & \dfrac{1}{2} \displaystyle\int_0^L [v'(x)]^2 \, dx = \varepsilon_0 \\ & v(\bar{x}) = A \end{cases} \quad (3.3)$$

where $\varepsilon_0 = \varepsilon|_{v(x)=v_0(x)}$ = constant since the strut is inextensible and the support will be held stationary after the initial end shortening $\varepsilon_0$ is applied.

Generally, the buckled shape of the strut can be approximated in the form of

$$v(x) = \sum_{j=1}^{N} Q_j \psi_j(x) \quad (3.4)$$

where $\psi_j(x)$ are shape functions consistent with the boundary conditions and the lateral constraint which are scaled by multipliers $Q_j$. Substituting this form of $v(x)$ into Eq. (3.3), the minimization problem becomes

$$\begin{cases} \min\limits_{Q_1,Q_2,\ldots} & U = \dfrac{1}{2}EI\displaystyle\int_0^L \left(\sum_{j=1}^{N} Q_j\psi_j''(x)\right)^2 dx \\ \text{subject to} & \dfrac{1}{2}\displaystyle\int_0^L \left(\sum_{j=1}^{N} Q_j\psi_j'(x)\right)^2 dx = \varepsilon_0 \\ & \displaystyle\sum_{j=1}^{N} Q_j\psi_j(\bar{x}) = A \end{cases} \tag{3.5}$$

which can be rewritten as

$$\begin{cases} \min\limits_{Q_1,Q_2,\ldots} & U = \dfrac{1}{2}\displaystyle\sum_{i=1}^{N}\sum_{j=1}^{N} k_{ij}Q_iQ_j \\ \text{subject to} & \displaystyle\sum_{i=1}^{N}\sum_{j=1}^{N} a_{ij}Q_iQ_j = \varepsilon_0 \\ & \displaystyle\sum_{j=1}^{N} Q_j\psi_j(\bar{x}) = A \end{cases} \tag{3.6}$$

where $k_{ij} = EI\int_0^L \psi_i''(x)\psi_j''(x)\,dx$ and $a_{ij} = \frac{1}{2}\int_0^L \psi_i'(x)\psi_j'(x)\,dx$.

A solution to the minimization problem is sought using a multiplier method, wherein multipliers $\mu$ and $\lambda$ are used to enforce the constraints. The end shortening equation is multiplied by $\mu$ and the lateral constraint equation by $\lambda$; the physical interpretation of these multipliers is discussed later. These equations are then appended to the strain energy equation to provide an augmented strain energy function, $U_a$, which will be maximized over the multipliers and minimized over the coefficients, as described in Eq. (3.7):

$$\begin{aligned} \min_{Q_1,Q_2,\ldots}\max_{\lambda,\mu} U_a = {} & \frac{1}{2}\sum_{i=1}^{N}\sum_{j=1}^{N} k_{ij}Q_iQ_j \\ & - \mu\left(\varepsilon_0 - \sum_{i=1}^{N}\sum_{j=1}^{N} a_{ij}Q_iQ_j\right) + \lambda\left(A - \sum_{j=1}^{N} Q_j\psi_j(\bar{x})\right) \end{aligned} \tag{3.7}$$

To find these optima, derivatives of $U_a$ with respect to each variable are set equal to

zero (i.e., the necessary conditions for optimality), leading leads to the following expressions:

$$\frac{\partial U_a}{\partial Q_i} = 0: \quad \sum_{j=1}^{N} k_{ij} Q_j + \left( 2 \sum_{j=1}^{N} a_{ij} Q_j \right) \mu - \psi_i(\bar{x}) \lambda = 0, \quad i = 1, \ldots, N \tag{3.8a}$$

$$\frac{\partial U_a}{\partial \mu} = 0: \quad \varepsilon_0 - \sum_{i=1}^{N} \sum_{j=1}^{N} a_{ij} Q_i Q_j = 0 \tag{3.8b}$$

$$\frac{\partial U_a}{\partial \lambda} = 0: \quad A - \sum_{j=1}^{N} Q_j \psi_j(\bar{x}) = 0 \tag{3.8c}$$

The roots of these $N + 2$ equations in terms of the coefficients $(Q_1, \ldots, Q_N)$ and multipliers $(\mu, \lambda)$ are sought.

It is desirable to select the shape functions $\psi_j(x)$ such that, when $A = H$, where $H$ is the initial rise of the buckled strut, $\psi_1(\bar{x}) = 1$ and all other $\psi_j(\bar{x}) = 0$. This results in $Q_1 = A$, since $v(\bar{x}) = A = H = Q_1 \psi_1(\bar{x})$, and the initial deformed shape of the strut $v_0(x)$ becomes $v_0(x) = H\psi_1(x)$. Therefore, the initial end shortening $\varepsilon_0$ can be written in terms of $H$ as follows:

$$\varepsilon_0 = \frac{1}{2} H^2 \int_0^L [\psi_1'(x)]^2 dx \equiv a_{11} H^2 \tag{3.9}$$

Since the lateral deflections are of interest for a BSVIS, it is convenient to express Eq. (3.8b) in terms of $H$ rather than $\varepsilon_0$, as follows:

$$a_{11} H^2 - \sum_{i=1}^{N} \sum_{j=1}^{N} a_{ij} Q_i Q_j = 0 \tag{3.10}$$

Thompson and Hunt (1983) observed that even though there are an infinite number of terms to the approximation of $v(x)$ (i.e, $N \to \infty$), retaining only two or three provides good agreement with experimental observations. In the following section (Section 3.2.1), two terms are retained to develop the stiffness of the negative stiffness region, and in the subsequent section (Section 3.2.2) three terms are retained for further exploration

of the load-deflection relation of the buckled strut.

### 3.2.1 Negative Stiffness Approximation with Two Terms

Retaining only two terms in the approximation of $v(x)$, Eq. (3.8a) can be written as a system of $N = 2$ equations in terms of $\mu$ and $\lambda$ as follows:

$$\begin{bmatrix} -\psi_1(\bar{x}) & 2a_{11}Q_1 + 2a_{12}Q_2 \\ -\psi_2(\bar{x}) & 2a_{12}Q_1 + 2a_{22}Q_2 \end{bmatrix} \begin{Bmatrix} \lambda \\ \mu \end{Bmatrix} = - \begin{Bmatrix} k_{11}Q_1 + k_{12}Q_2 \\ k_{12}Q_1 + k_{22}Q_2 \end{Bmatrix} \tag{3.11}$$

This system can be solved for $\lambda$, which is the value of the lateral force applied at $\bar{x}$ (Fig. 3.2(c)), and $\mu$, which is the value of the axial force applied to induce end shortening $\varepsilon_0$.

As stated earlier, it is convenient to select $\psi_1(x)$ and $\psi_2(x)$ such that $\psi_1(\bar{x}) = 1$ and $\psi_2(\bar{x}) = 0$. For the following discussion, a mid-span constraint is considered, that is, $\bar{x} = L/2$. It is additionally helpful to select $\psi_1(x)$ and $\psi_2(x)$ orthogonal to each other so that the cross-terms of the integrals (e.g., $k_{12}$ and $a_{12}$) become zero and only the pairing of a shape function with itself (e.g., $k_{11}$ and $a_{11}$) are left. If this is done, the system (3.11) simplifies to

$$\begin{bmatrix} -1 & 2a_{11}Q_1 \\ 0 & 2a_{22}Q_2 \end{bmatrix} \begin{Bmatrix} \lambda \\ \mu \end{Bmatrix} = - \begin{Bmatrix} k_{11}Q_1 \\ k_{22}Q_2 \end{Bmatrix} \tag{3.12}$$

Similarly, a solution for $Q_2$ in terms of $Q_1$ can be found from Eq. (3.10) as

$$Q_2 = \pm \sqrt{\frac{a_{11}}{a_{22}}(H^2 - Q_1^2)} \tag{3.13}$$

which describes an ellipse in $(Q_1, Q_2)$ space. Solutions for $Q_2$ therefore can take a positive or negative value for a given $A$.

From Eq. (3.12), a value is found for $\mu$, which is the force required to impose the end shortening $\varepsilon_0$:

$$\mu = -\frac{k_{22}}{2a_{22}} \tag{3.14}$$

This value is used to solve for $\lambda$, which is the value of the force applied at $\bar{x}$ to cause the

lateral deflection $A$, as a function of solely $Q_1$:

$$\lambda = -\left(\frac{a_{11}k_{22}}{a_{22}} - k_{11}\right)Q_1 \tag{3.15}$$

Since $Q_1 = A$, the terms in parentheses of Eq. (3.15) is the slope (or stiffness) of the negative stiffness portion of the lateral load-deflection ($\lambda$-$A$) relation, termed $k_{\text{neg}}$. Values of $k_{\text{neg}}$ have been evaluated and are tabulated in Table 3.1 for different conditions, referenced in the following as Cases a–d.

The combinations of boundary conditions and lateral constraints for Cases a–d are depicted in Figs. 3.3(a)–(d), respectively. Likewise, the $\psi_j(x)$ appearing in Table 3.1 are presented in Fig. 3.4. These shapes were selected based on the buckled shapes of columns with matching boundary conditions. In each case, $\psi_1$ corresponds to the first buckled mode shape of a column with fixed-fixed (Cases a and b) or pinned-pinned (Cases c and d) boundary conditions. For Cases b and c, $\psi_2$ corresponds to the second buckled mode shape of the respective columns. The $\psi_2$ chosen for Cases a and d is the first buckled mode shape of a pinned-fixed column for each half of the strut ($0 \leqslant x \leqslant L/2$). In Figs. 3.4(b) and (d), the right half of $\psi_2$ is mirrored below the support line (labeled as (ii)) because in the case of a perfect clamped constraint, there would be no communication between the two sides and they could theoretically take opposite orientations to one another. This is impossible with a knife-edge constraint since the constraint does not affect the slope of the strut, i.e., $v'(\bar{x}^-) = v'(\bar{x}^+)$.

The solution of the system for Cases a–c was relatively straightforward and yielded closed-form expressions for $k_{\text{neg}}$. Plots of $Q_2$ versus $Q_1$ are shown for each case in Fig. 3.5. The negative portion of the ellipse would correspond to an inverted $\psi_2$ in Fig. 3.4. The plots on the left of Fig. 3.5 show that as the lateral constraint is pushed down starting $A = H$, $v(x)$ would be expected to smoothly transition between values of $Q_1$ and $Q_2$, resulting in the load-deflection relations shown on the right of Fig. 3.5 with a

**Table 3.1:** Lateral negative stiffness values $k_{\text{neg}}$ for different boundary conditions and lateral constraints.

| Case | Boundary Conditions | Lateral Constraint | $\psi_1(x)$ | $\psi_2(x)$ | $k_{\text{neg}}$ |
|---|---|---|---|---|---|
| a | Fixed-Fixed | Knife-Edge | $\frac{1}{2}\left(1-\cos\frac{2\pi x}{L}\right)$ | $\frac{1}{C_{\mathsf{a}}}\left(\frac{x-l}{l}-kl\cos kl\right)\sin\frac{kl(x-l)}{l}$ † | $\frac{4.1830\pi^4 EI}{2L^3}$ |
| b | Fixed-Fixed | Clamped | $\frac{1}{2}\left(1-\cos\frac{2\pi x}{L}\right)$ | $\frac{1}{2}\left(1-\cos\frac{4\pi x}{L}\right)$ | $\frac{12\pi^4 EI}{2L^3}$ |
| c | Pinned-Pinned | Knife-Edge | $\sin\frac{\pi x}{L}$ | $\sin\frac{2\pi x}{L}$ | $\frac{3\pi^4 EI}{2L^3}$ |
| d | Pinned-Pinned | Clamped | $\sin\frac{\pi x}{L}$ | $\frac{1}{C_{\mathsf{d}}}\left(\frac{x}{l}-kl\cos kl\right)\sin\frac{klx}{l}$ † | $\frac{7.1830\pi^4 EI}{2L^3}$ ‡ |

†For Cases a and d, $\psi_2(x)$ is taken as the shape of a buckled pinned-fixed column (Chajes, 1974). In these equations, $l = L/2$, $kl$ is the solution of the transcendental problem $kl = \tan kl$, and $C_{\mathsf{a}}$ and $C_{\mathsf{d}}$ are the normalization constants to ensure $\psi_2$ has a unit amplitude

‡Value based on $\psi_2(x)$ rotationally symmetric about midspan, i.e., Case d(ii) in Fig. 3.4.

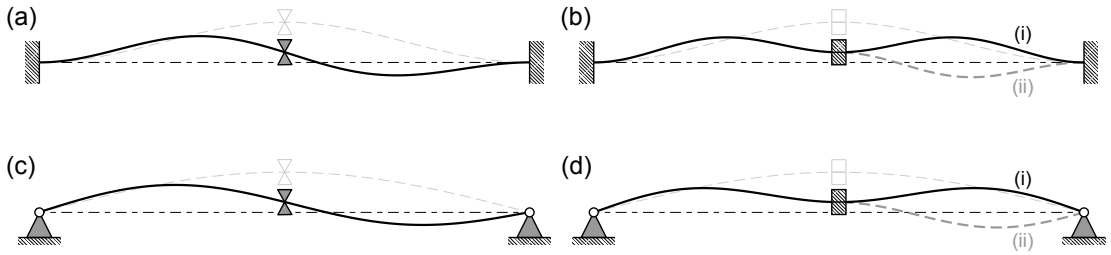



**Figure 3.3:** Boundary conditions and lateral constraints considered: fixed-fixed boundary conditions with (a) knife-edge and (b) clamped constraints, and pinned-pinned boundary conditions with (c) knife-edge and (d) clamped constraints. For cases b and d, the strut can assume either (i) symmetry or (ii) rotational symmetry about the clamped constraint at midspan.

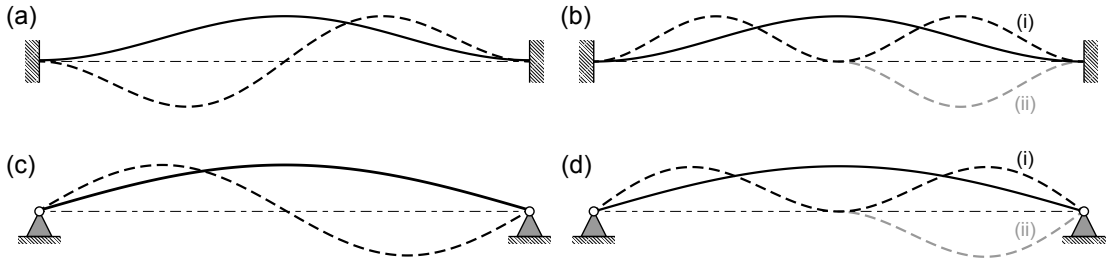



**Figure 3.4:** Shape functions $\psi_1(x)$ (——) and $\psi_2(x)$ (- - -) assumed in two-term expansion: fixed-fixed boundary conditions with (a) knife-edge and (b) clamped constraints, and pinned-pinned boundary conditions with (c) knife-edge and (d) clamped constraints. For cases b and d, $\psi_2(x)$ can be either (i) symmetric or (ii) rotationally symmetric about midspan.

constant slope of $-k_{\text{neg}}$. For these relations, the origin is at the level of the supports and the graphs begin at $A = H$, where the load is initially zero; i.e., these figures should be read from right ($A/H = +1$) to left ($A/H = -1$). As soon as load is applied, it jumps to the critical snap-through load found by a two-term approximation, which can be expressed as

$$\lambda_{cr} = -k_{\text{neg}} H \qquad \text{(2-term approx.)} \tag{3.16}$$

When the constraint is moved down (decreasing $A$), the magnitude of the load reduces as $A$ approaches zero and then becomes a positive load (i.e., the constraint must pull on the strut) after the constraint passes below the support line. Since the strut is inextensible and the supports do not translate after the initial end shortening, any movement of the constraint beyond $H$ would take an infinite load, either in compression or tension

depending on the direction of movement, as shown by the vertical lines at $A/H = \pm 1$.

The solution for Case d proved more difficult to resolve. The $Q_2$ versus $Q_1$ ellipse, shown in Fig. 3.5(c), is slightly rotated. This is because the shapes $\psi_1$ and $\psi_2$ for Case d(i) are not orthogonal in the end-shortening equation (i.e., $a_{12} = a_{21} \neq 0$). This yields two solutions for $Q_2$ when $Q_1 = H$: one in which $\psi_2 = 0$, and another where $\psi_2$ is nonzero. The load-deflection curves of Fig. 3.5 appear to cross, and one might expect a transition to be possible as in the other cases, but the two branches are completely detached from one another. When the solutions for the typical cases with $\psi_1$ and $\psi_2$ orthogonal to each other (e.g., Case c) and Case d(i) are plotted in $(Q_1, Q_2, \lambda)$ space (Figs. 3.6 and 3.7, respectively), the unique behavior of Case d(i) becomes more apparent. While the two branches of the solution for the typical cases are connected, no path connects the branches of the solution for Case d(i). Since the solution cannot go from one branch to the other, $\psi_2$ cannot disappear at $Q_1 = A$ and it becomes infinitely stiff. This solution is sensible when explained in terms of the moments and shears associated with Case d(i). In order to satisfy equilibrium when $v(\bar{x}) = 0$ (i.e., $Q_1 = 0$), the supports must provide a vertical reaction to balance the moment induced by the constraint. To balance these reactions, $\lambda$ must be non-zero, which is shown in Fig. 3.5(d) for Case d(i).

When $\psi_2$ for Case d(ii) is analyzed, these problems are resolved. The rotational symmetry results in the global orthogonality of $\psi_2$ to $\psi_1$. Also, equilibrium is now satisfied with $\lambda = 0$ when $v(\bar{x}) = 0$, because the configuration of the strut is such that any shears produced on the left side of the constraint are balanced by those on the right side. The resulting stiffness for Case d(ii) is reported in Table 3.1.

### 3.2.2 Load-Deflection Relation with Three Terms

In this section, the more-general development of the lateral load-deflection relation of a buckled strut presented in Section 3.2 is carried out for a three-term approximation of $v(x)$ for a pinned-pinned strut subjected to a knife-edge lateral constraint (Case c).

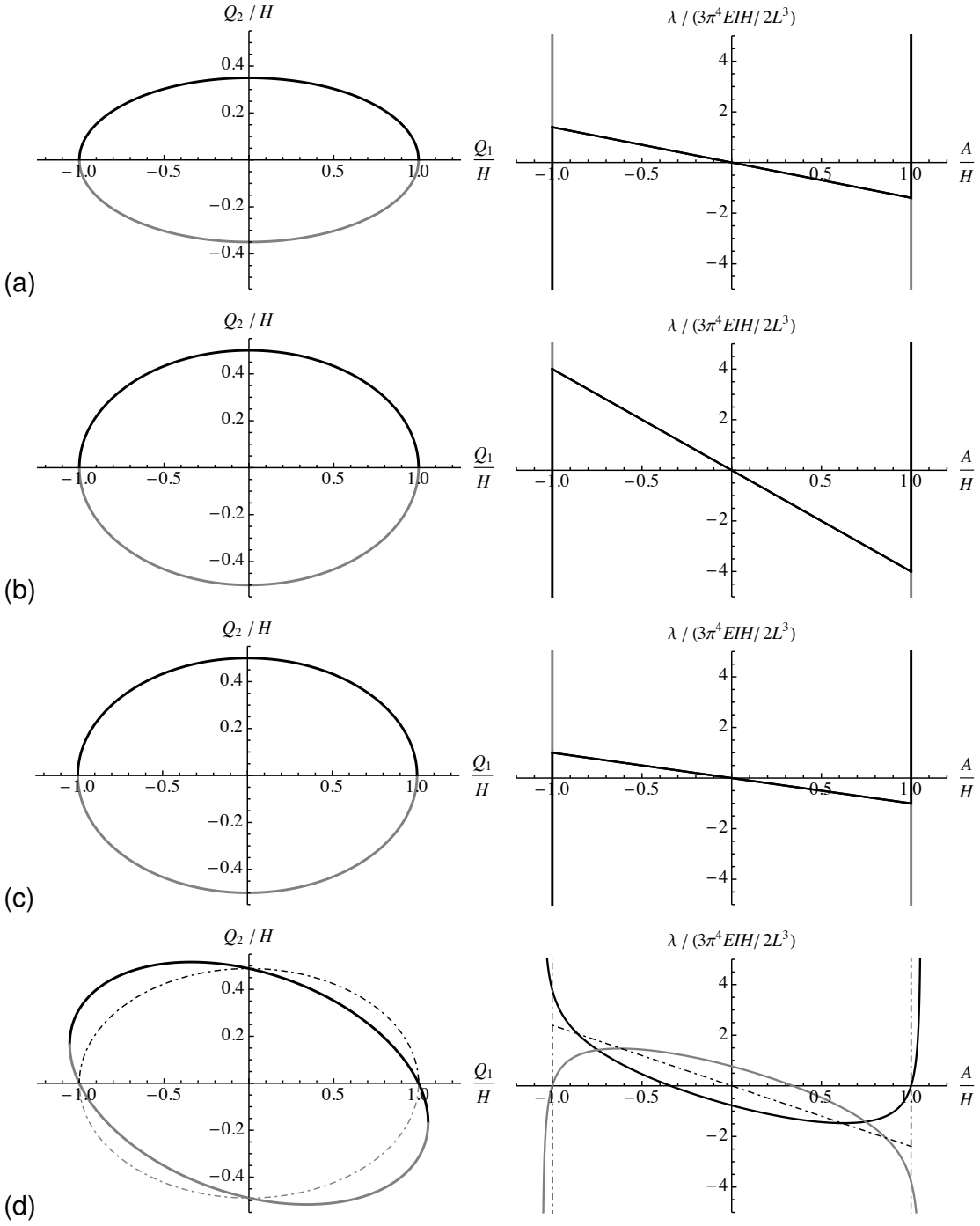



**Figure 3.5:** (left) Solutions for $Q_1$ and $Q_2$ normalized by rise $H$, and (right) the resulting load-deflection relations for Cases a–d (a–d). For Case d, both the symmetric (—) and rotationally symmetric (-·-·-) solutions are shown, corresponding to Cases d(i) and d(ii), respectively, in Fig. 3.4(d).

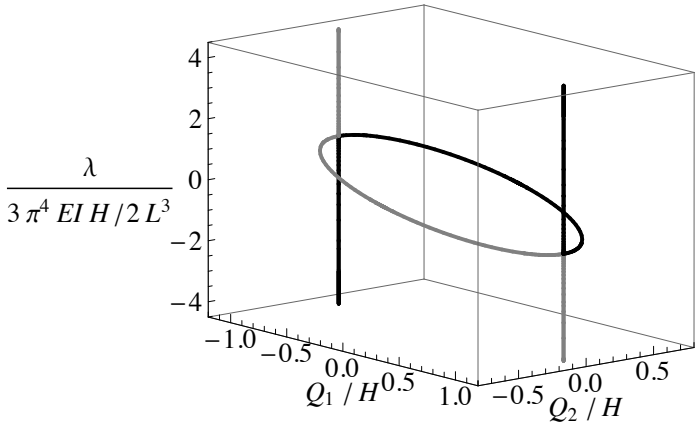



**Figure 3.6:** Load-deflection relations for Case c.

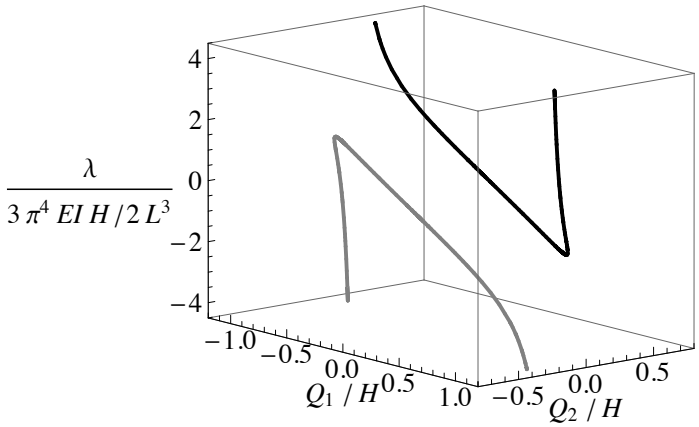



**Figure 3.7:** Detached load-deflection relations for Case d(i).

The effects of a linear spring are then incorporated into the system to give a model of a BSVIS in Section 3.3.

To obtain $\psi_1, \psi_2$ and $\psi_3$, a sum of Fourier harmonics is assumed for the lateral deflected shape:

$$v(x) = \sum_{n=1}^{\infty} Q_n \sin\left(\frac{n\pi x}{L}\right). \tag{3.17}$$

Retaining only the first three terms, Eq. (3.17) becomes

$$v(x) = Q_1 \sin\left(\frac{\pi x}{L}\right) + Q_2 \sin\left(\frac{2\pi x}{L}\right) + Q_3 \sin\left(\frac{3\pi x}{L}\right) \tag{3.18}$$

which relates to the first, second, and third buckling mode shapes of a pinned-pinned

column. Substituting this form of $v(x)$ into Eqs. (3.1) and (3.2), the integrals can be evaluated so that they become

$$U = \frac{1}{2}\frac{\pi^4 EI}{2L^3}\left(Q_1^2 + 16Q_2^2 + 81Q_3^2\right) \tag{3.19}$$

and

$$\varepsilon = \frac{1}{2}\frac{\pi^2}{2L}\left(Q_1^2 + 4Q_2^2 + 9Q_3^2\right). \tag{3.20}$$

It is important to note that, since the functions chosen for $\psi_n(x)$ are orthogonal to each other, the cross-terms of the general derivation all reduce to zero as in the two-term solutions.

The initial deformed shape of the buckled strut before the lateral constraint is imposed is a half sine wave, i.e., $v_0(x) = H\sin(\pi x/L)$. The corresponding end shortening $\varepsilon_0$ is

$$\varepsilon_0 = \frac{1}{2}\frac{\pi^2}{2L}H^2. \tag{3.21}$$

As in the general solution, the end shortening constraint is now expressed in terms of $H$ as follows:

$$\frac{1}{2}\frac{\pi^2}{2L}\left(Q_1^2 + 4Q_2^2 + 9Q_3^2\right) = \frac{1}{2}\frac{\pi^2}{2L}H^2. \tag{3.22}$$

With the assumed deflected shape of Eq. (3.18), the minimization problem of Eq. (3.6) now becomes

$$\begin{cases} \min\limits_{Q_1,Q_2,Q_3} & U = \frac{1}{2}C_1\left(Q_1^2 + 16Q_2^2 + 81Q_3^2\right) \\ \text{subject to} & \frac{1}{2}C_2\left(Q_1^2 + 4Q_2^2 + 9Q_3^2\right) = \frac{1}{2}C_2H^2 \\ & s_1Q_1 + s_2Q_2 + s_3Q_3 = A \end{cases} \tag{3.23}$$

where $C_1 \equiv k_{11} = \pi^4 EI/(2L^3)$, $C_2 \equiv a_{11} = \pi^2/(2L)$, and $s_n = \sin(n\pi\bar{x}/L)$. The constant $C_2/2$ is retained on either side of the end shortening equation because it is needed to

obtain the correct $\mu$, i.e., the axial force needed to produce the end shortening.

The constraints are augmented to the strain energy function using Lagrange multipliers $\lambda$ and $\mu$ as before. For $N = 3$ terms, the necessary conditions for optimality in Eqs. (3.8a)–(3.8c) become

$$0 = C_1 Q_1 + C_2 \mu Q_1 + \lambda s_1 \tag{3.24a}$$
$$0 = 16 C_1 Q_2 + 4 C_2 \mu Q_2 + \lambda s_2 \tag{3.24b}$$
$$0 = 81 C_1 Q_3 + 9 C_2 \mu Q_3 + \lambda s_3 \tag{3.24c}$$
$$\tfrac{1}{2} C_2 H^2 = \tfrac{1}{2} C_2 \left( Q_1^2 + 4 Q_2^2 + 9 Q_3^2 \right) \tag{3.24d}$$
$$A = s_1 Q_1 + s_2 Q_2 + s_3 Q_3. \tag{3.24e}$$

Solutions of this system of equations are equilibria which lie on the interface of the ellipsoid of Eq. (3.24d) and the plane of Eq. (3.24e), in $(Q_1, Q_2, Q_3)$ space. These can be found by solving Eqs. (3.24a)–(3.24c) for the Fourier coefficients, which yields

$$Q_1 = \frac{\lambda s_1}{C_1 + C_2 \mu} \tag{3.25a}$$
$$Q_2 = \frac{\lambda s_2}{4(4C_1 + C_2 \mu)} \tag{3.25b}$$
$$Q_3 = \frac{\lambda s_3}{9(9C_1 + C_2 \mu)} \tag{3.25c}$$

These can be substituted into Eqs. (3.24d) and (3.24e) to eliminate $\lambda$, resulting in a quartic polynomial in $\mu$. The roots for $\mu$ can be found and used to solve for the corresponding $\lambda$ and $Q_n$.

A test of stability is performed by analyzing the eigenvalues of the bordered Hessian matrix:

$$\mathbf{H}(U_a) = \begin{bmatrix} 0 & 0 & -a_{11} Q_1 & -a_{22} Q_2 & -a_{33} Q_3 \\ 0 & 0 & -\psi_1(\bar{x}) & -\psi_2(\bar{x}) & -\psi_3(\bar{x}) \\ -a_{11} Q_1 & -\psi_1(\bar{x}) & k_{11} + a_{11}\mu & 0 & 0 \\ -a_{22} Q_2 & -\psi_2(\bar{x}) & 0 & k_{22} + a_{22}\mu & 0 \\ -a_{33} Q_3 & -\psi_3(\bar{x}) & 0 & 0 & k_{33} + a_{33}\mu \end{bmatrix} \tag{3.26}$$

If more than two eigenvalues are less than zero, then the solution is unstable. For stable

solutions, the two negative eigenvalues of the bordered Hessian matrix correspond to the multipliers $\lambda$ and $\mu$, over which the augmented strain energy is maximized (see Eq. (3.7)).

The resulting lateral load-deflection ($\lambda$–$A$) relationship of the buckled strut is shown by the curves in Figs. 3.8(a)–(c) for varying $\bar{x}$. Stable branches are distinguished from unstable branches by the line style. These results can be interpreted similarly to the $\lambda$–$A$ plots of Fig. 3.5, beginning at $A = H$ and $\lambda = 0$ and progressively decreasing $A$. The load $\lambda$ decreases sharply to some minimum value, before snap-through (negative stiffness) behavior initiates. As $\bar{x}$ is placed further from midspan, this transition becomes more gradual and the minimum load is reduced in magnitude. No matter the location of $\bar{x}$, the minimum load is less than the $\lambda_{cr}$ found in the two-term approximation (i.e., $3\pi^4 EIH/2L^3$), and because some deflection occurs before the negative stiffness portion is reached, the negative stiffness found by the three-term approximation, denoted $\tilde{k}_{\text{neg}}$, is greater than the $k_{\text{neg}}$ found with two terms (Table (3.1)). The stiffness with the three-term approximation is given by

$$\tilde{k}_{\text{neg}} = \frac{\beta}{\alpha} k_{\text{neg}} \tag{3.27}$$

where $\alpha$ is the portion of $H$ over which the strut exhibits snap-through (negative-stiffness) behavior in the three-term approximation, and $\beta$ is the reduction (in magnitude) of the peak load relative to $\lambda_{cr}$. For $\bar{x} \approx 0.5L$ (Fig. 3.8(a)), these values are found to be 0.915 and 0.981, respectively, giving a 3-term negative stiffness of $\tilde{k}_{\text{neg}} = 1.072 k_{\text{neg}}$. These values will be used in the subsequent discussion of the BSVIS.

As $A$ approaches $-\alpha H$, the load follows the curve of the branch it began on until a vertical tangency is reached. At this point, the solution becomes unstable and it must "snap" to the nearest stable branch, which results in the path allowing a return to $\lambda = 0$ when $A = -H$. When $\bar{x}$ is very close to the center of the span (Fig. 3.8(a)), there is little

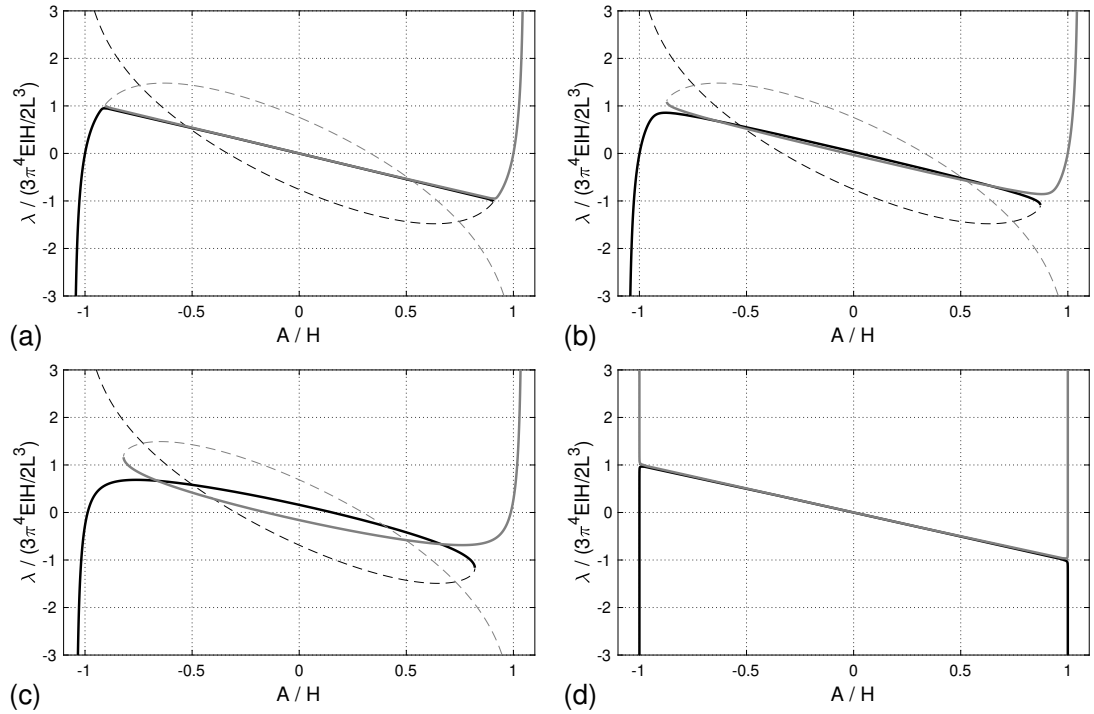



**Figure 3.8:** Normalized lateral load-deflection relation of a buckled strut for $\bar{x}$ = (a) $0.499L$, (b) $0.49L$, and (c) $0.45L$ using a three-term approximation of $v(x)$, as well as the two-term approximation for $\bar{x} = 0.499L$ (d). The black and gray lines are detached equilibria, each with stable (—) and unstable (– – –) branches.

jump to speak of, but the jump is more severe for larger eccentricities (Figs. 3.8(b) and (c)). For $A > H$ and $A < -H$, the load greatly increases due to the inextensibility of the strut.

## 3.3 Buckled-Strut Vertical Isolation System

To produce the desired BSVIS lateral load-deflection relation, a linear spring of stiffness $k = \kappa \tilde{k}_{\text{neg}}$, where $\kappa$ is the relative stiffness of the spring to the negative stiffness of the buckled strut, can be added in parallel with the strut (Fig. 3.1). With the addition of a spring, the total strain energy of the system becomes

$$U = \frac{1}{2} EI \int_0^L [v''(x)]^2 \, dx + \frac{1}{2} k [v(\bar{x}) - v_0(\bar{x})]^2. \tag{3.28}$$

Considering that the Fourier coefficients would appear in the spring energy term, this

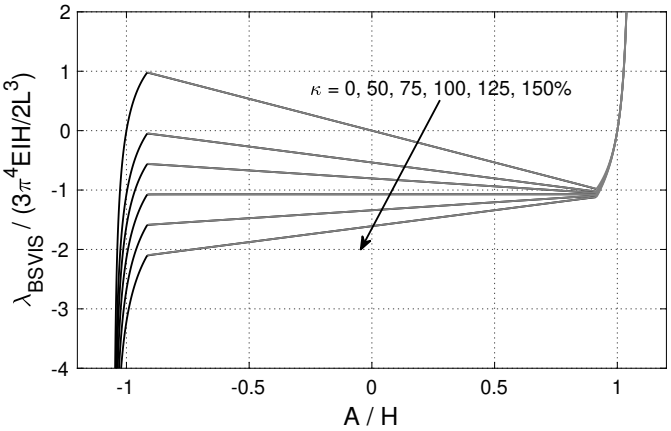



**Figure 3.9:** Normalized load-deflection relations of BSVISs composed of a pin-ended buckled strut (Case c with $\bar{x} \approx 0.5L$) in parallel with linear springs having different relative stiffnesses, $\kappa = k/\tilde{k}_{\text{neg}}$. Unstable solutions are not shown.

formulation requires a more-involved solution than what has been presented. However, the effect can be assumed to be small and it is considered a reasonable approximation to superimpose the spring force to the solution for $\lambda$ to attain the force produced by a BSVIS $\lambda_{\text{BSVIS}}$ as follows:

$$\lambda_{\text{BSVIS}} = \lambda + k(A - H) \equiv \lambda + \kappa\tilde{k}_{\text{neg}}(A - H) \tag{3.29}$$

This effect is plotted in Fig. 3.9 for springs of varying $\kappa$, and the results are discussed here.

Starting again at $A = H$, the constraint is moved down (decreasing $A$), and the load decreases sharply. The load where the snap-through behavior begins is relatively unchanged by $\kappa$. Therefore, this transition load will be assumed constant, taken to be $\lambda_{cr} = 3\pi^4 EIH/2L^3$, in the following discussion. Beyond this load, the load-deflection relation is approximately linear given by

$$\lambda_{\text{BSVIS}} = -\tilde{k}_{\text{neg}}A + k(A - H) \equiv (\kappa - 1)\tilde{k}_{\text{neg}}A - \kappa\tilde{k}_{\text{neg}}H, \quad -\alpha H \leqslant A \leqslant \alpha H \tag{3.30}$$

Recall $\alpha$ is the portion of $H$ over which the strut exhibits snap-through (negative-stiffness) behavior. The introduction of the spring results in an effective stiffness for

the snap-through portion of the curve of

$$k_{\text{BSVIS}} = k - \tilde{k}_{\text{neg}} \equiv (\kappa - 1)\tilde{k}_{\text{neg}} \tag{3.31}$$

If $\kappa = 1$, the system has zero effective stiffness for the snap-through portion. A system with $\kappa \gtrsim 1$ has low positive stiffness, desirable for vibration isolation (Calhoun and Harvey, 2018). If $\kappa < 1$, the negative stiffness of the snap-through behavior of the strut still dominates, and the system would not be able to effectively support or isolate a mass.

It is apparent in Fig. 3.9 that the load at which snap-through (negative-stiffness) behavior ends (i.e., at $A = -\alpha H$) is shifted downwards as relative stiffness $\kappa$ increases. This transitional load is equal to

$$\lambda_{\text{BSVIS}}\Big|_{A=-\alpha H} = -(\kappa - 1)\tilde{k}_{\text{neg}}\alpha H - \kappa\tilde{k}_{\text{neg}}H \equiv -[(\kappa - 1)\alpha + \kappa]\tilde{k}_{\text{neg}}H \tag{3.32}$$

Considering a payload of mass $m$ to settle vertically to the center ($A = 0$) under its dead weight, the settlement would be $H$, and the balancing load from the BSVIS would equal

$$\lambda_{\text{BSVIS}}\Big|_{A=0} = -mg \Rightarrow mg = \kappa\tilde{k}_{\text{neg}}H \equiv kH \tag{3.33}$$

The device would have a displacement operating range of $Y = \pm\alpha H$ about $A = 0$ and a tolerance to changes in weight of the payload of $\pm(\kappa - 1)\tilde{k}_{\text{neg}}\alpha H$. Note that for $\kappa = 1$ ($k_{\text{BSVIS}} = 0$), there is no tolerance for misidentifying the payload weight, which is not practical; therefore, $\kappa$ should be taken to be greater than 1.

### 3.3.1 BSVIS Benefits

Consider the schematic of the BSVIS load-deflection relation shown in Fig. 3.10, where the BSVIS stiffness $k_{\text{BSVIS}}$ has been determined to be effective for vibration isolation. The benefit of the BSVIS can be demonstrated by considering the vertical settlement of a linear spring with similar effects (settlement or effective stiffness). First, consider a

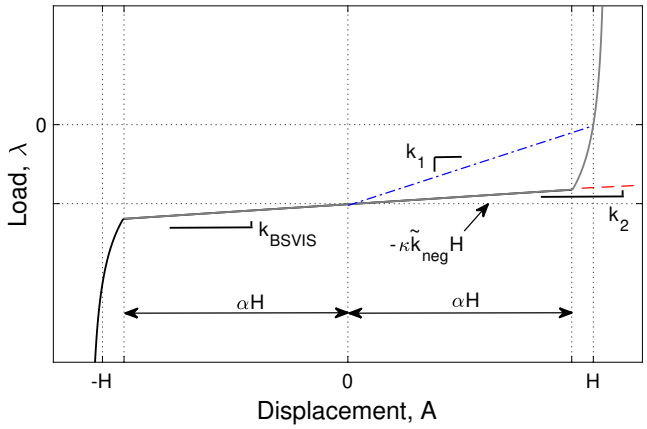



**Figure 3.10:** BSVIS load-deflection relationship.

spring that would achieve the same low-profile settlement as the BSVIS (i.e., the initial rise of the strut $H$) for a payload of mass $m$. Such a spring would need to be selected to have a stiffness of

$$k_1 = \frac{mg}{H} = \kappa\tilde{k}_{\text{neg}} = \frac{\kappa}{\kappa - 1}k_{\text{BSVIS}} \tag{3.34}$$

This would result in an undesirably stiff system for isolation purposes. For example, for a value of $\kappa = 1.5$, the required stiffness would be $k_1 = 3k_{\text{BSVIS}}$, corresponding to a 73% increase in frequency; these results are more dramatic as $\kappa$ approaches unity. Alternatively, consider a spring having the desired stiffness $k_2 = k_{\text{BSVIS}}$. To support the same payload mass, this spring would settle (or compress)

$$\Delta A = \frac{1}{k_2}mg = \frac{1}{(\kappa - 1)\tilde{k}_{\text{neg}}}\kappa\tilde{k}_{\text{neg}}H = \frac{\kappa}{\kappa - 1}H \tag{3.35}$$

This would result in undesirably large settlements, requiring an isolation system not possessing a low-profile. For example, for a value of $\kappa = 1.5$, the settlement would be $3H$, corresponding to a profile that is three times taller. From these results, it is clear that a BSVIS provides the desired low stiffness with a small settlement allowing for a low-profile design.

## 3.4 BSVIS Prototype

A prototype, pictured in Fig. 3.11, was developed to experimentally characterize the behavior of the BSVIS, validate the theory of Section 3.3, and prove the attainability of this device. 3D-printed beams of length $L$ = 177.8 mm whose flexural rigidity $EI$ were determined in our previous work as 83,000 N·m$^2$ (see Porter et al. (2019), Specimen 3) were used for the strut. The expected negative stiffness $\tilde{k}_{\text{neg}}$ with these values is 2.31 N/mm. Connections were designed to approximate the behavior of a pin and used to hold the strut in a rigid frame consisting of T-slotted framing that allowed for easy manipulation of the end shortening. The uprights of the frame were held in place by brackets and 0.794-mm (1/32-in.) shims. One of these shims could be removed from each side of the uprights to allow for increments of 1.588 mm (1/16 in.) of end shortening while keeping the device centered. A platform was fabricated using 3D printing to interface with a universal testing machine for static testing or support a payload for dynamic testing (see Section 4.2). The platform was also designed to connect to linear springs to provide the counteracting positive stiffness while avoiding collision with the strut during testing. Two extension springs were chosen for the prototype for the sake of constructability since it was relatively easy to attach extension springs to the T-slotted framing and a compression spring would have presented a greater challenge. Each spring had a stiffness of 0.215 N/mm, resulting in a total spring stiffness $k$ = 0.430 N/mm and $\kappa$ = 0.186. The spring-to-platform connections were designed so the platform could be centered and the T-slotted framing could act as a linear guide and prevent excessive rotation of the platform. The platform connected to the strut through a 3D-printed piece designed to approximate the knife-edge lateral constraint condition. Finally, for static tests, a bracket was fabricated for connecting the rigid frame to the base of the testing machine.

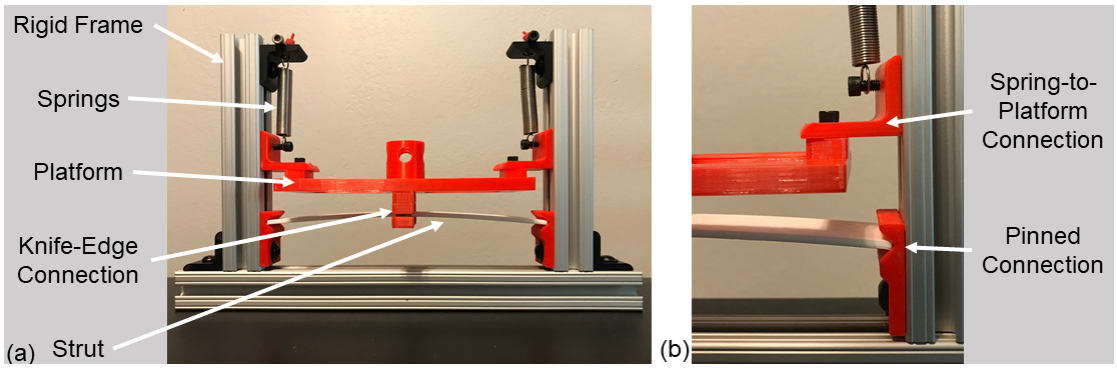



**Figure 3.11:** Photograph of the prototype of a BSVIS (a) various components labeled and (b) close-up of the pinned connection and the spring-to-platform connection

## 3.5 Experimental Results

### 3.5.1 Static Testing

For static testing, the prototype was connected to a universal testing machine (Fig. 3.12). The load cell of the testing machine was connected to the platform interface with no load when the strut was at its initial rise $H$ (approximately 7.5 mm) and the constraint was centered on the strut ($\bar{x} = 0.5L$). This point is the origin of the experimental data, so experimentally measured deflection would need to be shifted by the rise $H$ to correspond directly to the theoretical graphs. The BSVIS was loaded at a constant displacement rate to 11 mm and then reversed to 5 mm. This cycle was repeated five times. This testing process was conducted twice for the BSVIS without springs connected and twice with springs connected. For the tests without springs, the test was run out to 15 mm of extension after the cycles were completed; for the tests with springs, it was stopped after the cycles. Experimental data from these tests are presented in Fig. 3.13. Stiffness found by fitting the data of different portions of the load-deflection relations are denoted on the plots. In Fig. 3.13(a), it is apparent that the buckled strut displayed strong negative stiffness behavior in the snap-through region and the relation follows the same general shape that is expected theoretically. It is also apparent that the springs did stiffen the system when they were connected. The differences in slopes at the start of loading

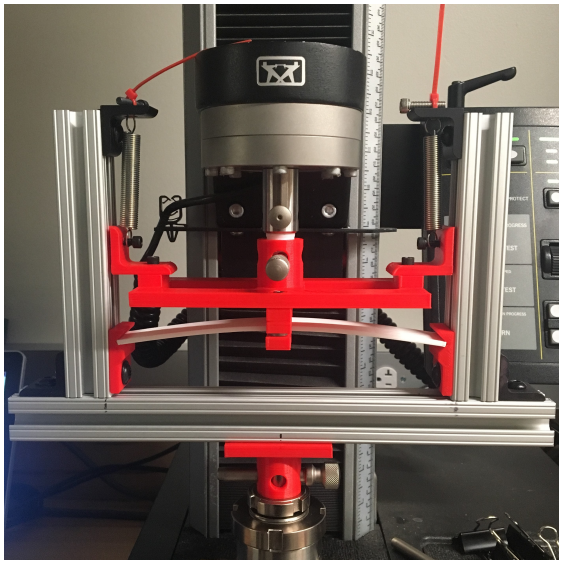


**Figure 3.12:** Photograph of the BSVIS prototype shown connected to the universal testing machine

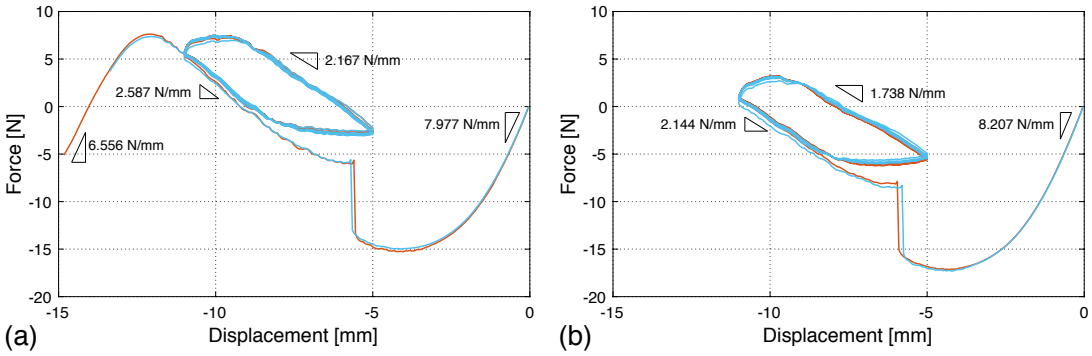



**Figure 3.13:** Experimental load deflection data for tests (a) without and (b) with springs connected. Slopes for different portions of the relations are denoted on each plot

is 0.23 N/mm due to the springs. The differences in the loops are 0.429 N/mm and 0.443 N/mm for the "top" and "bottom" of the loops respectively. Recall that the total spring stiffness $k$ used in these tests was 0.430 N/mm, so these differences due to the connection of the springs prove that the linear superposition of the spring and buckled-strut forces (Eq. (3.29)) is valid for the snap-through region.

An unexpected effect than what is predicted in Section 3.3 is that the data show a difference between entering and exiting the snap-through region. Prior to reaching the snap-through region, the load increases and, rather than smoothly transitioning to snap-

through behavior, it exhibits a large jump at a deflection of about 6 mm from a larger-magnitude load to the smaller-magnitude load in the snap-through region. This jump corresponded to the deflected shape of the strut suddenly switching from exhibiting first- and third-mode effects to being second-mode dominated. This is thought to be a result of the assumption that the strut is inextensible, when in actuality, the strut is able to undergo small axial deformation. The axial deformation allows the strut to realize a higher load than is possible in the perfectly inextensible case (Thompson and Hunt, 1983). It is seen that after the strut buckles into the second-mode-dominated shape, the load-deflection relation is continuous and has a linear slope (stiffness). Also observed in Fig. 3.13(a) is that the load smoothly transitions out of the negative stiffness region and quickly returns to zero. If the loading cycles had been conducted across the full extension range, it is expected that a similar rise in load and subsequent jump down into the snap-through region would have occurred progressing from maximum deflection to zero deflection.

An additional difference between the theory and the experiment is the opening up of the hysteretic loops when the cycles were conducted. Friction between the support brackets and the ends of the strut could have contributed a portion of this. Additionally, note that Fig. 3.8 shows a distancing of the stable solutions for increasing $\bar{x}$. While the lateral constraint was centered on the strut, some error in the precise location is to be expected. Fig. 3.8(c) shows a not insubstantial opening of a loop for $\bar{x} = 0.45L$, which could be thought of as being ±5% off-center. For a strut of $L = 177.8$ mm, the lateral constraint would only need to be off-center by ±8.9 mm to realize this condition. The experimental data could show connection between the two stable branches of the theoretical solution within $-\alpha H \leqslant A \leqslant \alpha H$. This would also explain the difference of stiffness between the top and bottom of the loops. In Fig. 3.8(c), each branch of the solution is not linear in the snap-through region, but rather has a slight curvature, with

the magnitude of the slope increasing along a branch as it nears the vertical tangency where it becomes unstable. Therefore, for $-H \leqslant A \leqslant 0$, $\tilde{k}_{\text{neg}}$ of the top branch is smaller than $\tilde{k}_{\text{neg}}$ of the bottom branch. This effect is observed in Fig. 3.13 when the stiffnesses of the top and bottom branches are compared. A non-centered loading also may account for some of the difference in the predicted $\tilde{k}_{\text{neg}}$ and the measured negative stiffnesses in that $\alpha$ and $\beta$ change with $\bar{x}$.

Discrepancies between theoretical predictions and experimental results can also be attributed to the relatively high rise of the experimental prototype. Eqs. (3.1) and (3.2) are simplified considering the initial rise of the strut $H$ to be shallow. In the assembly of the prototype, the strut attained a relatively large initial rise (about 4% of its length), potentially rendering this approximation imprecise.

## 3.6 Design Recommendations

A designer may intend to protect a certain piece of equipment from vertical seismic motions by engineering an isolation system with a very low stiffness. A simple design procedure for a BSVIS given the mass of any such payload $m$, a desired stiffness $k_{\text{BSVIS}}$, and a desired displacement range $Y$ is presented in this section. The theoretical BSVIS load-deflection relations of Section 3.3 predict an operating range $Y = \pm\alpha H$ about the static equilibrium point for a BSVIS. While more experimental data will provide further confirmation of these predictions (see Section 4.2), the data presented in Section 3.5 confirm the negative-stiffness behavior of a buckled strut and that the inclusion of a positive stiffness spring in parallel with the buckled strut alters the overall stiffness of the system in a predictable manner. Therefore, a design based on the theoretical predictions is reasonable.

Using a specified displacement range $Y$, one can find the necessary rise $H = Y/2\alpha$. Eq. (3.33) can now be solved for the required linear spring stiffness $k$ to support the payload:

$$k = \frac{mg}{H} \tag{3.36}$$

Using Eq. (3.31), a required lateral stiffness of the strut $\tilde{k}_{\text{neg}}$ can be determined as

$$\tilde{k}_{\text{neg}} = k - k_{\text{BSVIS}} \tag{3.37}$$

The lateral stiffnesses $k_{\text{neg}}$ listed in Table 3.1 can be used to design a strut based on desired boundary conditions and constraint types for the desired BSVIS using Eq. (3.27). For the design of a pin-ended, knife-edge BSVIS corresponding to Case c (such as the prototype BSVIS), values of $\alpha = 0.915$ and $\beta/\alpha = 1.072$ are recommended. Values for $\alpha$ and $\beta$ can be developed for the other cases following a similar procedure.

To summarize, the design of a BSVIS given a payload of mass $m$, a desired stiffness $k_{\text{BSVIS}}$, and an operating displacement range $Y$ follows these steps:

1. Find $H = Y/2\alpha$.
2. Select a linear spring of stiffness $k = mg/H$.
3. Determine the required lateral stiffness of the buckled strut $\tilde{k}_{\text{neg}} = k - k_{\text{BSVIS}}$.
4. Select boundary conditions and a lateral constraint type.
5. Using Table 3.1, design a strut with $EI$ and $L$ such that $\tilde{k}_{\text{neg}} = \beta k_{\text{neg}}/\alpha$ is satisfied.

The prototype developed should not be thought of as a basis for design, because of the tall profile the extension springs require. To achieve a lower profile, the positive stiffness could be provided by compression springs as shown in Fig. 3.1 or leaf springs supporting the platform for the payload.

## 3.7 Summary

In this chapter, a buckled-strut vertical isolation system (BSVIS) was proposed. The lateral load-deflection relation of a buckled strut, which provides the negative stiffness

for a BSVIS, was developed for a general case, and evaluated for different two-term approximations to extract values of the negative stiffness provided by such systems. A three-term approximation was then carried out to more-accurately predict the behavior of a BSVIS, which was obtained by adding a linear spring into the model. The nonlinear effects of a BSVIS offer considerable benefits for achieving vertical isolation over using linear springs. A prototype BSVIS was fabricated and subjected to limited static testing, which proved the validity of the prediction of negative stiffness for a pin-ended strut subjected to a knife-edge lateral constraint. The experiments also proved that the approximation in Eq. (3.29), which is that the linear spring force can be superimposed to provide the force of the BSVIS, is suitable. It is expected that use of springs of larger relative stiffness $\kappa$ would likewise alter the stiffness of the system and an isolation-level positive stiffness is attainable. Based on the theoretical development and experimental observations, a design guide for a BSVIS to support a given payload was presented.

# Chapter 4
# Summary, Conclusions, and Future Work

## 4.1 Summary and Conclusions

This thesis opened with a presentation of related literature on the topic of seismic protection and using negative stiffness to induce elastic nonlinearities in Chapter 1. In Chapter 2, a novel smooth negative stiffness device (SNSD) was presented for the seismic mitigation of structures through apparent weakening. A theoretical load-deflection relation was developed for this SNSD, and a prototype was fabricated to achieve this relation. The prototype was installed in an experimental structure, which was subjected to static, harmonic, and white noise tests, confirming the non-linear behavior induced by the SNSD. Simulations were conducted for the experimental parameters that showed good agreement with the experimental results. Simulations were then carried out for different possible configurations of SNSDs in an inelastic structure under various ground motions. These simulations further proved the effectiveness of an SNSD to achieve apparent weakening. Chapter 3 presented the development of a buckled-strut vertical isolation system (BSVIS) for the protection of components within buildings from vertical ground motions. Theoretical stiffnesses were developed for various boundary conditions and lateral constraints, and the case of a pin-ended strut with a knife-edge constraint was further developed. The load-deflection relation of a BSVIS was attained by integrating a linear spring into this model, and an experimental prototype was characterized by static tests, validating the theoretical predictions. The investigations into

both devices demonstrated that geometric nonlinearities can be engineered to passively reduce adverse effects of seismic events with advantages over linear systems.

## 4.2 Future Work

This research is an advancement in knowledge of elastic nonlinear systems for passive seismic mitigation. As a continuation of this research, the following are several areas which have the potential for further investigation:

- The requirements of a large pretensioned spring and long rotating lever arms still exist in the proposed SNSD design, and this may be a drawback in the construction of a full-scale device. Additionally, while the use of a cable-pulley system overcomes some of the drawbacks of a rack-and-pinion device (see Section 1.3.1), the radii of the pulleys is linearly related to the maximum desired displacement of the structure. In civil structures, desired deflections are relatively small compared to story height, so the radii of the pulleys according to the current design must be small, resulting in high stresses in the pulley shaft. Further research should be conducted into areas of different designs that could reduce these drawbacks.

- The BSVIS proposed here was only characterized by preliminary experimental tests. The static tests can be expanded to capture the entire hysteresis of the load-deflection relation, both for the entire range of deflection and for the operating range in the snap-through portion. Dynamic tests should also be conducted to characterize the performance of the BSVIS for vertical isolation. The theory can also be expanded to consider dynamic effects and conduct simulations of an isolated system. Tests can also be performed with alternate boundary conditions and lateral constraints to confirm the theoretical stiffnesses developed in the two-term approximations.

# Bibliography


AISC (2016). *Specification for Structural Steel Buildings, ANSI/AISC 360-16*. American Institute of Steel Construction, Chicago, IL (June 22).

Araki, Y., Asai, T., and Masui, T. (2009). "Vertical vibration isolator having piecewise-constant restoring force." *Earthquake Engineering & Structural Dynamics*, 38(13), 1505–1523. doi:10.1002/eqe.915.

ASCE (2017). *Minimum Design Loads and Associated Criteria for Buildings and Other Structures*. American Society of Civil Engineers (ASCE), ASCE/SEI 7-16 edition.

Attary, N., Symans, M., and Nagarajaiah, S. (2017). "Development of a rotation-based negative stiffness device for seismic protection of structures." *Journal of Vibration and Control*, 23(5), 853–867. doi:10.1177/1077546315585435.

Cain, T. M. N., Harvey, Jr, P. S., and Walsh, K. K. (2020). "Modeling, characterizing, and testing a simple, smooth negative-stiffness device to achieve apparent weakening." *Journal of Engineering Mechanics*. doi:10.1061/(ASCE)EM.1943-7889.0001823.

Calhoun, S. J. and Harvey, Jr., P. S. (2018). "Enhancing the teaching of seismic isolation using additive manufacturing." *Engineering Structures*, 167, 494–503. doi:10.1016/j.engstruct.2018.03.084.

Chajes, A. (1974). *Principles of Structural Stability Theory*. Prentice-Hall, Inc.

Chen, L., Sun, L., and Nagarajaiah, S. (2015). "Cable with discrete negative stiffness device and viscous damper: passive realization and general characteristics." *Smart Structures and Systems*, 15(3), 627–643. doi:10.12989/sss.2015.15.3.627.

Cimellaro, G. P., Domaneschi, M., and Warn, G. (2018). "Three-dimensional base isolation using vertical negative stiffness devices." *Journal of Earthquake Engineering*, 1–29. doi:10.1080/13632469.2018.1493004.

Fichter, W. and Pinson, M. W. (1989). "Load-shortening behavior of an initially curved eccentrically loaded column." *NASA Technical Memorandum 101643*, National Aeronautics and Space Administration, Hampton, VA (December).

Gavin, H. P. (2017). "The Levenberg-Marquardt method for nonlinear least squares curve-fitting problems." *Department of Civil and Environmental Engineering, Duke University*, <http://people.duke.edu/~hpgavin/lm.pdf>.

Gavin, H. P. and Dickinson, B. W. (2011). "Generation of uniform-hazard earthquake ground motions." *Journal of Structural Engineering*, 137, 423–432. doi: 10.1061/(ASCE)ST.1943-541X.0000331.

Harvey, Jr., P. S. (2015). "Vertical accelerations in rolling isolation systems: Experiments and simulations." *Journal of Engineering Mechanics*, 142(3), 04015091. doi:10.1061/(ASCE)EM.1943-7889.0001017.

Harvey, Jr, P. S. and Cain, T. M. N. (2020). "Buckling of elastic columns with initial imperfections and load eccentricity." *Structures*, 23, 660–664. doi:10.1016/j.istruc. 2019.09.021.

Harvey, Jr., P. S., Heinrich, S. K., and Muraleetharan, K. K. (2018). "A framework for post-earthquake response planning in emerging seismic regions: An oklahoma case study." *Earthquake Spectra*, 34(2), 503–525. doi:10.1193/053117EQS100M.

Harvey, Jr., P. S. and Kelly, K. C. (2016). "A review of rolling-type seismic isolation: Historical development and future directions." *Engineering Structures*, 125, 521–531. doi:10.1016/j.engstruct.2016.07.031.

Harvey, Jr., P. S. and Virgin, L. N. (2015). "Coexisting equilibria and stability of a shallow arch: Unilateral displacement-control experiments and theory." *International Journal of Solids and Structures*, 54, 1–11. doi:10.1016/j.ijsolstr.2014.11.016.

Harvey, Jr., P. S., Virgin, L. N., and Tehrani, M. H. (2019). "Buckling of elastic columns with second-mode imperfections." *Meccanica*, 1245(8), 1245–1255. doi: 10.1007/s11012-019-01025-z.

Iemura, H. and Pradono, M. H. (2009). "Advances in the development of pseudo-negative-stiffness dampers for seismic response control." *Structural Control and Health Monitoring*, 16(7-8), 784–799. doi:10.1002/stc.345.

Ioakimidis, N. I. (2018). "The energy method in problems of buckling of bars with quantifier elimination." *Structures*, 13, 47–65. doi:10.1016/j.istruc.2017.08.002.

Kashdan, L., Conner Seepersad, C., Haberman, M., and Wilson, P. (2012). "Design, fabrication, and evaluation of negative stiffness elements using SLS." *Rapid Prototyping Journal*, 18(3), 194–200. doi:10.1108/13552541211218108.

Kelly, J. M., Skinner, R. I., and Heine, A. J. (1972). "Mechanisms of energy absorption in special devices for use in earthquake resistant structures." *Bulletin of NZ Society for Earthquake Engineering*, 5(3), 63–88.

Klasson, A., Crocetti, R., and Hansson, E. F. (2016). "Slender steel columns: How they are affected by imperfections and bracing stiffness." *Structures*, 8, 35–43. doi: 10.1016/j.istruc.2016.08.004.

Lee, C.-M., Goverdovskiy, V. N., and Temnikov, A. I. (2007). "Design of springs with "negative" stiffness to improve vehicle driveer vibration isolation." *Journal of Sound and Vibration*, 302(4), 865–874. doi:10.1016/j.jsv.2006.12.024.

Lee, D. and Constantinou, M. C. (2018). "Combined horizontal–vertical seismic isolation system for high-voltage–power transformers: development, testing and validation." *Bulletin of Earthquake Engineering*, 16(9), 4273–4296. doi:10.1007/s10518-018-0311-2.

Levenberg, K. A. (1944). "A method for the solution of certain non-linear problems in least squares." *Quarterly of Applied Mathematics*, 2, 164–168.

Madah, H. and Amir, O. (2018). "Concurrent structural optimization of buckling-resistant trusses and their initial imperfections." *International Journal of Solids and Structures*, 162, 244–258. doi:10.1016/j.ijsolstr.2018.12.007.

Moroni, M. O., Sarrazin, M., and Soto, P. (2012). "Behavior of instrumented base-isolated structures during the 27 February 2010 Chile earthquake." *Earthquake Spectra*, 28(1_suppl1), 407–424. doi:10.1193/1.4000041.

Pasala, D. T. R., Sarlis, A. A., Nagarajaiah, S., Reinhorn, A. M., Constantinou, M. C., and Taylor, D. (2013). "Adaptive negative stiffness: New structural modification approach for seismic protection." *Journal of Structural Engineering*, 139(7), 1112–1123. doi:10.1061/(ASCE)ST.1943-541X.0000615.

Pasala, D. T. R., Sarlis, A. A., Reinhorn, A. M., Nagarajaiah, S., Constantinou, M. C., and Taylor, D. (2014). "Simulated bilinear-elastic behavior in a SDOF elastic structure using negative stiffness device: Experimental and analytical study." *Journal of Structural Engineering*, 140(2), 04013049. doi:10.1061/(ASCE)ST.1943-541X.0000830.

Platus, D. L. (1992). "Negative-stiffness-mechanism vibration isolation systems." *Vibration Control in Microelectronics, Optics, and Metrology*, Vol. 1619, 44–54, <https://doi.org/10.1117/12.56823>.

Plaut, R. and Mráz, Z. (1992). "Uni-directional buckling of a pinned elastica with external pressure." *International Journal of Solids and Structures*, 29(16), 2091–2100. doi:10.1016/0020-7683(92)90196-Z.

Plaut, R. H., Dillard, D. A., and Virgin, L. N. (2006). "Postbuckling of elastic columns with second-mode imperfections." *Journal of Engineering Mechanics*, 132(8), 898–901. doi:10.1061/(ASCE)0733-9399(2006)132:8(898).

Polymaker (2017). *PolyLite$^{TM}$ PLA Technical Data Sheet*. Polymaker (June).

Porter, J. H., Cain, T. M., Fox, S. L., and Harvey, Jr., P. S. (2019). "Influence of infill properties on flexural rigidity of 3D-printed structural members." *Virtual and Physical Prototyping*, 14(2), 148–159. doi:10.1080/17452759.2018.1537064.

Robinson, W. H. and Tucker, A. G. (1976). "A lead-rubber shear damper." *Bull. New Zealand Natl. Soc. Earthquake Engrg*, 4, 251–259.

Ryan, K. L., Soroushian, S., Maragakis, E., Sato, E., Sasaki, T., and Okazaki, T. (2016). "Seismic simulation of an integrated ceiling-partition wall-piping system at e-defense. i: Three-dimensional structural response and base isolation." *Journal of Structural Engineering*, 142(2), 04015130. doi:10.1061/(ASCE)ST.1943-541X.0001384.

Saaed, T. E., Nikolakopoulos, G., Jonasson, J.-E., and Hedlund, H. (2015). "A state-of-the-art review of structural control systems." *Journal of Vibration and Control*, 21(5), 919–937. doi:10.1177/1077546313478294.

Sarlis, A. A., Pasala, D. T. R., Constantinou, M. C., Reinhorn, A. M., Nagarajaiah, S., and Taylor, D. P. (2013). "Negative stiffness device for seismic protection of structures." *Journal of Structural Engineering*, 139(7), 1124–1133. doi: 10.1061/(ASCE)ST.1943-541X.0000616.

Soong, T. T. (1988). "State-of-the-art review: Active structural control in civil engineering." *Engineering Structures*, 10(2), 74–84. doi:10.1016/0141-0296(88)90033-8.

Spencer, Jr, B. F. and Sain, M. K. (1997). "Controlling buildings: a new frontier in feedback." *IEEE Control Systems*, 17, 19–35. doi:10.1109/37.642972.

Symans, M. D., Charney, F. A., Whittaker, A. S., Constantinou, M. C., Kircher, C. A., Johnson, M. W., and McNamara, R. J. (2008). "Energy dissipation systems for seismic applications: Current practice and recent developments." *Journal of Structural Engineering*, 134(1), 3–21. doi:10.1061/(ASCE)0733-9445(2008)134:1(3).

Thompson, J. M. T. and Hunt, G. W. (1983). "On the buckling and imperfection-sensitivity of arches with and without prestress." *International Journal of Solids and Structures*, 19(5), 445–459. doi:10.1016/0020-7683(83)90055-0.

Virgin, L. N. (2018a). "Enhancing the teaching of elastic buckling using additive manufacturing." *Engineering Structures*, 174, 338–345. doi:10.1016/j.engstruct.2018.07.059.

Virgin, L. N. (2018b). "Tailored buckling constrained by adjacent members." *Structures*, 16, 20–26. doi:10.1016/j.istruc.2018.08.005.

Walsh, K. K., Boso, E., Steinberg, E. P., Haftman, J. T., and Littell, W. N. (2018). "Variable negative stiffness device for seismic protection of building structures through apparent weakening." *Journal of Engineering Mechanics*, 144(9), 04018090. doi:10.1061/(ASCE)EM.1943-7889.0001512.

Warn, G. P. and Ryan, K. L. (2012). "A review of seismic isolation for buildings: Historical development and research needs." *Buildings*, 2, 300–325. doi: 10.3390/buildings2030300.

Zhou, Y., Chen, P., and Mosqueda, G. (2019). "Analytical and numerical investigation of quasi-zero stiffness vertical isolation system." *Journal of Engineering Mechanics*, 145(6), 04019035. doi:10.1061/(ASCE)EM.1943-7889.0001611.

# Appendix A

# Buckling under Imperfections[†]

## A.1 Background

Euler buckling theory assumes that, among other assumptions, the member is perfectly straight and that the compressive load is through the neutral axis at every cross section. Initial member imperfections and load eccentricities, however, are unavoidable in practice (Klasson et al., 2016; Madah and Amir, 2018; AISC, 2016, Comm. 1.2). Both member imperfections and load eccentricity have the effect of inducing bending as soon as the load is applied, gradually at low compressive load and more rapidly when the load approaches the critical value for the perfect column (Plaut and Mráz, 1992). While these two imperfections manifest in a similar manner, they are often treated separately (Chajes, 1974). In practice, these imperfections can be engineered to produce a soft post-buckling behavior for isolation as in the study by Fichter and Pinson (1989), but they considered only the case in which the imperfections compounded to further enhance the softening behavior, concluding that the load eccentricity is easier to impose with accuracy.

This chapter investigates column behavior if member imperfection and load eccentricity are simultaneously present. Pinned members are analyzed assuming linearly

[†]This chapter is published as Harvey and Cain (2020).

elastic, slender, uniform, and inextensible columns. A linear analysis based on Euler-Bernoulli theory is performed to compare the relative significance of member imperfections and load eccentricity on the deflected shape. The theoretical results are experimentally validated with the help of additive manufacturing (or 3D printing) (Virgin, 2018a; Porter et al., 2019). 3D printing provides an accurate and versatile means of seeding imperfections into a test specimen to promote, or control, its buckling characteristics (Virgin, 2018b; Harvey et al., 2019). A series of initially imperfect specimens with eccentric load application points are tested, exhibiting imperfection amplification and cancellation. Good agreement is seen between the theoretical predictions and the experimental results.

The material in this chapter emphasizes phenomenological behavior. Attention is focused on the canceling effect of initial member imperfections and load eccentricity in which the direction of the midspan deflection switches. There are a number of ways the analysis can be made more general (e.g., assuming different forms of the initial imperfection (Harvey et al., 2019; Plaut et al., 2006) and/or different boundary conditions (Ioakimidis, 2018)), but this study focuses on pinned columns with member imperfections that take the shape of the first buckling mode.

## A.2 Initially Bent, Eccentrically Loaded Column

Consider a prismatic pin-ended column of length $L$ with flexural rigidity $EI$ under axial load $P$ applied eccentrically at $e$; see Fig. A.1. The column has an initial camber of amplitude $a$, assumed to be a half sine wave (i.e., the first buckling mode):

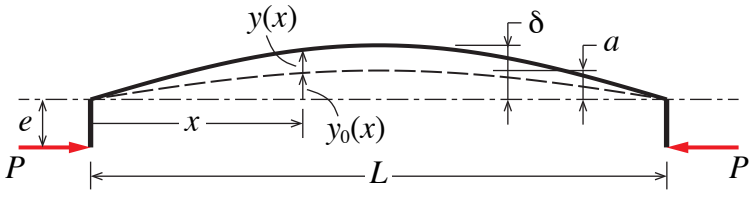



**Figure A.1:** Initially bent column under eccentric load.

$y_0(x) = a\sin(\pi x/L)$. Assuming the slope is small, the differential equation governing the deflected shape $y(x)$ is given by

$$EIy''(x) + Py(x) = -Pa\sin(\pi x/L) - Pe \tag{A.1}$$

The general solution to this equation is

$$y(x) = A\sin kx + B\cos kx + \frac{P/P_{cr}}{1 - P/P_{cr}} a\sin(\pi x/L) - e \tag{A.2}$$

where $k = \sqrt{P/EI}$ and the Euler buckling load $P_{cr} = \pi^2 EI/L^2$. The coefficients $A$ and $B$ are found from the boundary conditions $y(0) = y(L) = 0$, giving

$$y(x) = \frac{1 - \cos kL}{\sin kL} e\sin kx + e\cos kx + \frac{P/P_{cr}}{1 - P/P_{cr}} a\sin(\pi x/L) - e \tag{A.3}$$

### A.2.1 Effect of Imperfections on Midspan Deflection

The total deflection $\delta$ at midspan is given by

$$\delta = y(L/2) + y_0(L/2) \equiv \frac{a}{1 - P/P_{cr}} + e\Big[\sec\Big(\frac{\pi}{2}\sqrt{P/P_{cr}}\Big) - 1\Big] \tag{A.4}$$

Note that, as defined, a positive amplitude $a$ (in the absence of load eccentricity) would give a positive midspan deflection $\delta$; likewise, a positive load eccentricity $e$ (in the absence of initial camber) would result in a positive deflection $\delta$. Therefore, if both $a$ and $e$ are positive, the beam deflection $\delta$ surely will be positive (Plaut and Mráz, 1992). Of interest here is the case in which the signs of the amplitude $a$ and eccentricity $e$ are opposite, which raises the following questions: What happens if the signs of the amplitude $a$ and eccentricity $e$ are opposite? Additionally, in which direction would the column buckle?

To answer these question, the sign of the deflection $\delta$ is tracked as the load $P$ approaches the Euler buckling load $P_{cr}$. To wit, consider the following limit:

$$\lim_{P/P_{cr}\to 1} \delta = (a + 4e/\pi)\infty \tag{A.5}$$

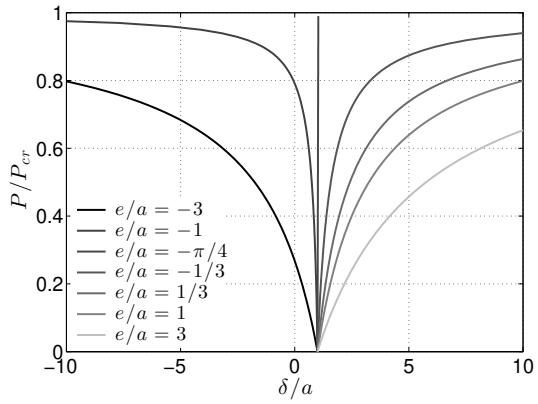



**Figure A.2:** Load-deflection curves of eccentrically loaded, pre-cambered columns.

Clearly, the direction of the deflection depends on the sign of this limit, which depends linearly on $a$ and $e$. Of interest is where the sign of the deflection switches, i.e., the zero crossing of the term in parenthesis:

$$a + 4e/\pi = 0 \Rightarrow \frac{e}{a} = -\frac{\pi}{4} \approx -0.7854 \tag{A.6}$$

As expected, the switching occurs when $e$ and $a$ have opposite sign. At this critical $e/a$ ratio, the imperfections from load eccentricity and initial camber cancel each other out, resulting in what is effectively the Euler buckling scenario. The behavior on either side of this singularity is characterized as follows:

$$\delta \begin{cases} < 0: & e/a < -\pi/4 \quad \text{(eccentricity controls)} \\ = 0: & e/a = -\pi/4 \quad \text{(neutralized)} \\ > 0: & e/a > -\pi/4 \quad \text{(camber controls)} \end{cases} \tag{A.7}$$

Figure A.2 gives a graphical representation of Eq. (A.4). The variation of $\delta/a$ with $P/P_{cr}$ is shown plotted for seven values of $e/a$, including the critical value of $e/a = -\pi/4$. Comparison of the curves shows that for $e/a < -\pi/4$ negative deflections result as $P$ approaches $P_{cr}$. Conversely, for $e/a > -\pi/4$, the deflections end up positive as $P$ approaches $P_{cr}$.

To better understand how these imperfections manifest in terms of the lateral deflec-

tion, Eq. (A.4) can be expanded using a Taylor series as follows:

$$\delta = a\left[1 + \frac{P}{P_{cr}} + \left(\frac{P}{P_{cr}}\right)^2 + \cdots\right] + e\left[\frac{\pi^2}{8}\frac{P}{P_{cr}} + \frac{5\pi^4}{384}\left(\frac{P}{P_{cr}}\right)^2 + \cdots\right] \tag{A.8}$$

At zero load, the deflection is independent of the load eccentricity, i.e., $\delta|_{P=0} = a$. Comparing the coefficients on the linear terms $O(P/P_{cr})$, the sensitivity on eccentricity $e$ (i.e., $\pi^2/8$) is about 23% greater than that of amplitude $a$ (i.e., 1). Hence, the deflection $\delta$ is more sensitive to eccentricity, which is similarly true for the higher-order terms in the series; this is why the critical eccentricity-to-amplitude ratio found in Eq. (A.6) is less than 1. It is worth noting that the critical eccentricity-to-amplitude ratio for the first-order term is $e/a = -8/\pi^2 \approx -0.8106$, which is greater than the value found in Eq. (A.6). Hence, the deflection $\delta$ is less sensitive to eccentricity $e$ as load $P$ approaches the critical load $P_{cr}$.

## A.3 Experiments

As discussed in the previous section, as the ratio of load eccentricity $e$ to imperfection amplitude $a$ increases, the deflection at midspan changes sign, and it is this switching of sign that is the focus of this study. A series of simple tests was performed to illustrate this behavior and its dependence on the ratio $e/a$.

### A.3.1 Experimental Setup

Relatively slender columns were fabricated with a consumer-grade 3D printer (Taz 6, Lulzbot, Loveland, CO). The specimens were printed out of PolyLite PLA (Polymaker, 2017). The "standard" (default) settings were used in the slicing software (Cura v21.08) for all specimens. The test specimens were designed to easily allow for varying load application points and initial imperfection amplitude. The design is shown in Fig. A.3(a). The clear span length $L$ was held constant for all specimens. Three initial imperfection amplitudes were used: $a$ = 3.175, 6.350, and 9.525 mm. The three 3D-printed test

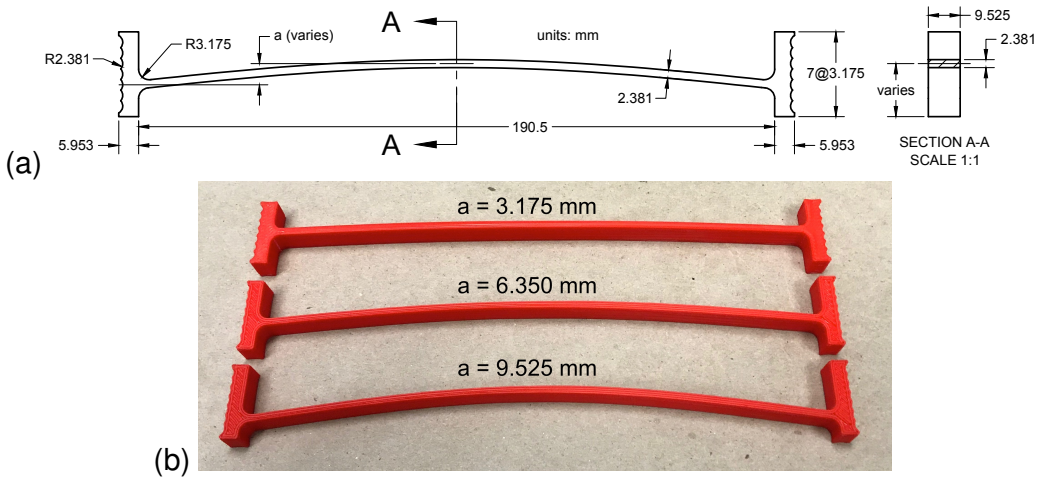



**Figure A.3:** (a) Test specimen nominal dimensions and (b) 3D-printed specimens.

specimen are shown in Fig. A.3(b).

The ends of the columns were integrated into rigid load application mechanisms. Small fillets were incorporated to avoid stress concentrations at the interface of the column and load application mechanism, and the height of the interface varied with the amplitude to ensure a large enough range of eccentricities could be tested. The load application mechanisms were designed with seven evenly spaced loading points that mated with rotary loading pins to mimic friction-free pinned boundary conditions (see Fig. A.4). Each pin fixtures was composed of a loading pin between mounted ball bearings. The pin fixtures were attached to the load heads in a Universal Testing Machine (5543, Instron, Norwood, MA) equipped with a load cell to measure the applied axial load. The compressive load was measured simultaneously with the end shortening during the displacement-controlled load tests; the load rate was 10 mm/min to a maximum end shortening of 10 mm. While the lateral deflection $\delta$ was not measured, the sign of the midspan deflection at the end to the tests (10-mm end shortening) was noted, which is of interest here.

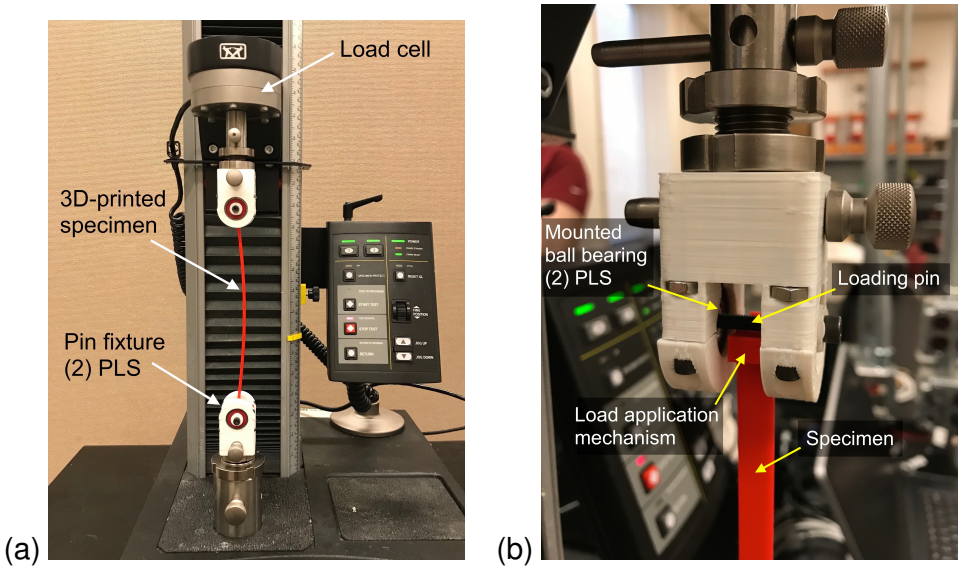



**Figure A.4:** Images of the experimental setup (a) and pin fixture (b).

### A.3.2 Experimental Results

The results presented here focus on the sign of the midspan deflection with varying $e/a$ ratios. As $e/a$ increases, $\delta$ is expected to change sign at $e/a \approx -0.7854$ (see Eq. (A.6)), switching from *eccentricity controlled* ($\delta < 0$) to *camber controlled* ($\delta > 0$). In Fig. A.5, the compressive load $P$ is plotted versus end shortening for the three imperfection amplitudes: $a$ = (a) 3.175, (b) 6.350, and (c) 9.525 mm. The line color distinguishes the $e/a$ ratio. Note that the $e/a$ resolution varies with the initial imperfection, with increments of 1, 1/2, and 1/3 for $a$ = 3.175, 6.350, and 9.525 mm, respectively. As the $e/a$ ratio increases, the load-deflection curves initially stiffen (approaching the "perfect" Euler buckling case), reaching a stiffest case, and then soften. The stiffest cases correspond to $e/a = -1$, $-1$, and $-2/3$ for the three cases considered, which is in good agreement with the theory (see Fig. A.2). For the largest amplitude used ($a$ = 9.525 mm, Fig. A.5(c)), the stiffness is nearly the same for $e/a = -1$ and $-2/3$; this is expected because these two cases straddle the critical $e/a$ ratio of $-0.7854$, with $e/a = -2/3$ being slightly stiffer (closer to the critical value).

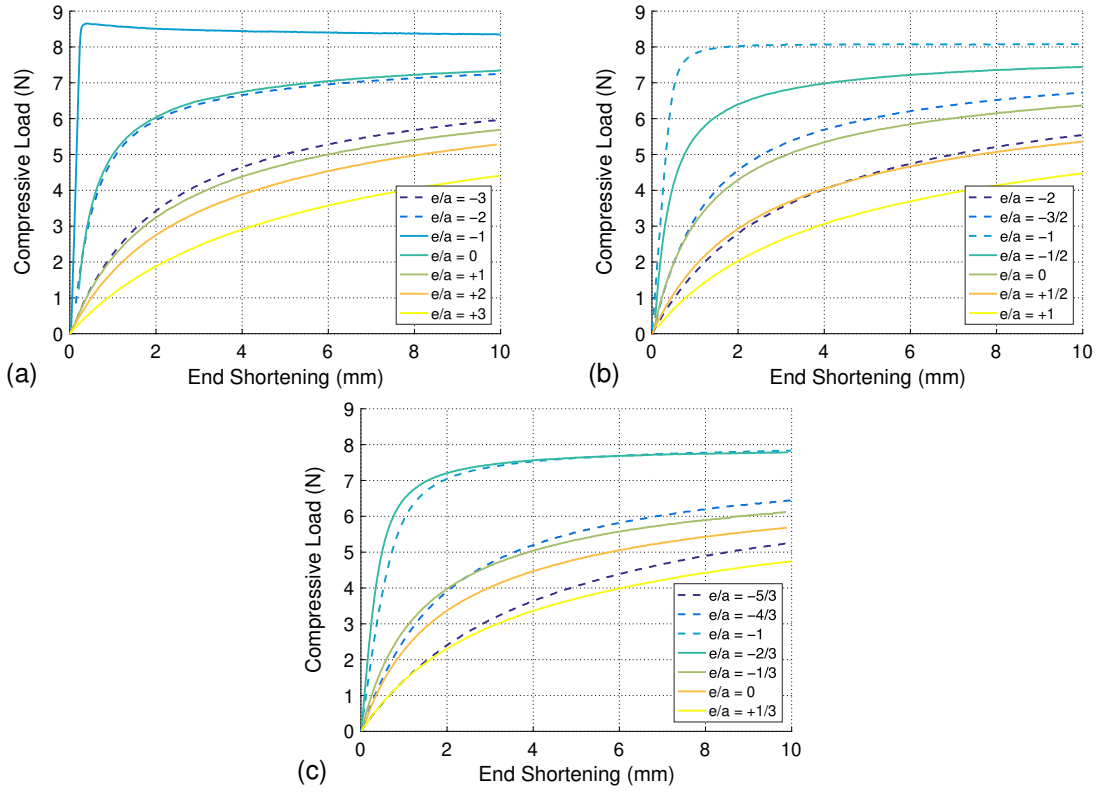



**Figure A.5:** Compressive load versus end shortening for imperfection amplitude $a$ = (a) 3.175, (b) 6.350, and (c) 9.525 mm with varying load eccentricity to imperfection amplitude ratio $e/a$. Sign of midspan deflection is distinguished by line style: $\delta < 0$ (dashed) and $\delta > 0$ (solid).

The transition from stiffening to softening correlates with the sign of the midspan deflection. In Fig. A.5, sign of the midspan deflection is distinguished by the line style. In all cases but $a = 3.175$ mm (Fig. A.5(a)), the midspan deflection is negative (i.e., eccentricity controlled) for $e/a \leqslant -1$, while the midspan deflection is positive (i.e., camber controlled) for $e/a > -1$. For the smallest imperfection amplitude ($a = 3.175$ mm, Fig. A.5(a)), the stiffest case corresponded to a ratio of $e/a = -1$, with a load-deflection curve that closely resembles Euler buckling (i.e., almost vertical path).

The data in Fig. A.5 are recast in Fig. A.6 to better illustrate the influence of $e/a$ on the sign of the midspan deflection. With load eccentricity $e$ plotted against imperfection amplitude $a$, the theory (based on Eq. (A.7)) predicts that the sign of the midspan deflection will switch at $e = -\frac{\pi}{4}a$, separating regions of negative deflection (eccentricity

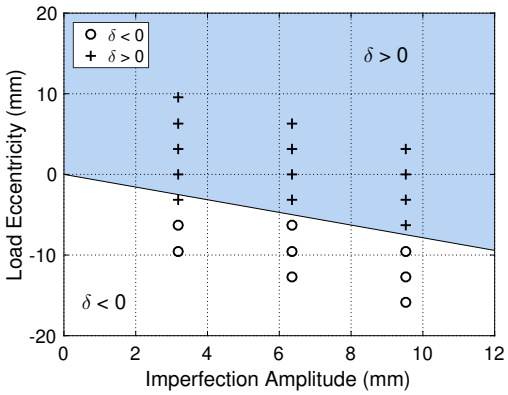



**Figure A.6:** Regions of positive and negative midspan deflection $\delta$ in the parametric space (load eccentricity $e$ versus imperfection amplitude $a$) based on Eq. (A.7), with comparison to experimental results ($\delta < 0$: $\circ$; $\delta > 0$: $+$).

controlled) and positive deflection (camber controlled). The data (distinguished by the marker) corresponds well with the theory. The only exception, as previously discussed, was for the smallest imperfection amplitude ($a = 3.175$ mm, Fig. A.5(a)), in which the $e/a$ resolution is coarsest.

### A.3.3 A Note on Repeatability

Two additional specimens were printed with imperfection amplitude $a = 3.175$ mm to test the repeatability of the results, in particular the case of $e/a = -1$ which deflected opposite the theory (see Fig. A.6). The specimens were subjected to the same loading sequence (positive $e/a$ to negative $e/a$). For the load case of $e/a = -1$, one specimen had a positive deflection, and the other specimen had a negative deflection. Therefore, 1/3 of the specimens deflected according to the theory, while the other 2/3 deflected opposite the theory.

The original specimen was tested an additional 10 times—5 oriented concave to the left, and 5 oriented concave to the right—at $e/a = -1$ with the specimen removed and reset between each test; in all cases the column's deflection was controlled by the eccentricity ($\delta < 0$), as predicted by the theory. Hence, the first test of the original specimen at $e/a = -1$ was not in keeping with the average response, indicating better

agreement with the theory than originally determined. It is worth noting that, after the numerous tests the original specimen was subjected to, it may have slightly plastic deformed, resulting in a bias to deflecting repeatedly into the eccentricity-controlled shape. This highlights the close proximity of this particular test to the cusp between imperfection-controlled and eccentricity-controlled equilibria.

### A.3.4 Circular Arc Initial Imperfection

Tests were also conducted on similar specimen that had imperfections in the form of circular arcs (instead of the first buckling mode, i.e., half sine) with the same imperfection amplitudes. While the geometric imperfection follows a different form than was assumed in Section A.2, these circular arcs exhibited the same qualitative behavior shown in Fig. A.6. The results are not presented here, but the theoretical justification for the similarity is due to a (shallow) circular arc being similar to the first buckling mode, discussed here.

The equation of a circular arc is

$$y_0(x) = \sqrt{R^2 - (x - L/2)^2} - \sqrt{R^2 - (L/2)^2} \tag{A.9}$$

where $R = [a^2 + (L/2)^2]/(2a)$. This equation can be expanded in terms of a Fourier series

$$y_0(x) = \sum_{n=1}^{\infty} a_n \sin \frac{n\pi x}{L} \tag{A.10}$$

where the Fourier coefficients are given by

$$a_n = \frac{\int_0^L y_0(x) \sin \frac{n\pi x}{L} dx}{\int_0^L \sin^2 \frac{n\pi x}{L} dx} \equiv \frac{2}{L} \int_0^L y_0(x) \sin \frac{n\pi x}{L} dx \tag{A.11}$$

The even coefficients ($n = 2, 4, 6, ...$) are all zero because the circular arc is symmetric about midspan ($x = L/2$, for the selected origin). The first four odd coefficients are tabulated in Table A.1 for representative geometries considered in this study. In all

**Table A.1:** Fourier coefficients $a_n$ ($n = 1, 3, 5, 7$) for a circular arc with span $L = 190.5$ mm and varying amplitude $a$.

| $a$ (mm) | $a_1$ (mm) | $a_3$ (mm) | $a_5$ (mm) | $a_7$ (mm) |
|---|---|---|---|---|
| 3.175 | 3.27725 | 0.121963 | 0.0263543 | 0.00960537 |
| 6.350 | 6.55748 | 0.247533 | 0.053556 | 0.0195265 |
| 9.525 | 9.84365 | 0.380316 | 0.0824834 | 0.0300941 |

three cases, the first Fourier coefficient is about 26 times larger than the third, so the circular arc can be approximated accurately by the just first term in the series.

## A.4 Concluding Remarks

This chapter has considered the combined effects of initial member imperfections and load eccentricities on static equilibrium configurations of pinned columns. In particular, the dependence of the sign (direction) of the midspan lateral deflection on the ratio of load eccentricity $e$ and imperfection amplitude $a$ was studied. At the critical ratio of $e/a = -\pi/4$, the sign of the midspan deflection switches, separating two distinct responses: eccentricity controlled ($e/a < -\pi/4$) and imperfection controlled ($e/a > -\pi/4$). Measurements (compressive load and end shortening) were made on 3D-printed columns with different load eccentricities and initial cambers. The data were able to span the range from eccentricity controlled to imperfection controlled, showing good agreement with the theoretical predictions.